Bioactive Materials 20 (2023) 472–488

Contents lists available at ScienceDirect

Bioactive Materials

journal homepage: www.keaipublishing.com/en/journals/bioactive-materials

Microenvironment-responsive electrocution of tumor and bacteria by implants modified with degenerate semiconductor film

Donghui Wang [a,b,1], Shun Xing [a,e,1], Feng Peng [c], Xianming Zhang [a], Ji Tan [a], Xueqing Hao [b], Yuqin Qiao [a], Naijian Ge [d,**], Xuanyong Liu [a,f,*]

[a] State Key Laboratory of High Performance Ceramics and Superfine Microstructure, Shanghai Institute of Ceramics, Chinese Academy of Sciences, Shanghai, 200050, China
[b] School of Health Sciences and Biomedical Engineering, Hebei University of Technology, Tianjin, 300130, China
[c] Department of Orthopedics, Guangdong Provincial People's Hospital, Guangdong Academy of Medical Sciences, Guangzhou, Guangdong, 510080, China
[d] Intervention Center, Eastern Hepatobiliary Surgery Hospital, The Third Affiliated Hospital of Naval Medical University, Shanghai, 200438, China
[e] Center of Materials Science and Optoelectronics Engineering, University of Chinese Academy of Sciences, Beijing, 100049, China
[f] School of Chemistry and Materials Science, Hangzhou Institute for Advanced Study, University of Chinese Academy of Sciences, 1 Sub-lane Xiangshan, Hangzhou, 310024, China

ARTICLE INFO

Keywords:
Electrotherapy
Implant
Layered double hydroxides
Anti-Tumor
Antibiosis

ABSTRACT

Implantable biomaterials are widely used in the curative resection and palliative treatment of various types of cancers. However, cancer residue around the implants usually leads to treatment failure with cancer reoccurrence. Postoperation chemotherapy and radiation therapy are widely applied to clear the residual cancer cells but induce serious side effects. It is urgent to develop advanced therapy to minimize systemic toxicity while maintaining efficient cancer-killing ability. Herein, we report a degenerate layered double hydroxide (LDH) film modified implant, which realizes microenvironment-responsive electrotherapy. The film can gradually transform into a nondegenerate state and release holes. When in contact with tumor cells or bacteria, the film quickly transforms into a nondegenerate state and releases holes at a high rate, rendering the "electrocution" of tumor cells and bacteria. However, when placed in normal tissue, the hole release rate of the film is much slower, thus, causing little harm to normal cells. Therefore, the constructed film can intelligently identify and meet the physiological requirements promptly. In addition, the transformation between degenerate and nondegenerate states of LDH films can be cycled by electrical charging, so their selective and dynamic physiological functions can be artificially adjusted according to demand.

1. Introduction

Cancer is now the leading cause of death in wealthy countries. In the past half-century, the incidence of cancer has been increasing year by year. If the trend continues, researchers predict cancer could become the top killer worldwide [1]. However, humans have not found an effective way to cure cancer completely. Resect the malignant lesions through surgery is the first treatment option for tumors without extensive metastatic lesions, while palliative therapy is the optimal choice for terminal cancer [2]. Implants are widely used in both cases, they can fill the surgical site resulting from the tumor resection surgery [3,4]. Or as a stent to alleviate malignant obstruction in the palliative treatment [5,6]. For example, the golden strategy for osteosarcoma therapy is surgery to remove tumor tissues and fill the defects with implants; stents are widely used in palliation treatment of obstruction of trachea, bronchi, esophagus, and bile duct induced by various cancers. However, cancer residues inevitably exist, and these uncleared cancer cells are prone to colonize around the implant, leading to cancer recurrence, metastasis after the surgical treatment, and re-obstruction in the palliative treatment. Therefore, patients have to suffer from postoperative adjuvant

Peer review under responsibility of KeAi Communications Co., Ltd.
* Corresponding author. State Key Laboratory of High Performance Ceramics and Superfine Microstructure, Shanghai Institute of Ceramics, Chinese Academy of Sciences, Shanghai, 200050, China.
** Corresponding author.
E-mail addresses: gelarge@163.com (N. Ge), xyliu@mail.sic.ac.cn (X. Liu).
[1] **These authors contributed equally to this work.**

https://doi.org/10.1016/j.bioactmat.2022.06.004
Received 25 March 2022; Received in revised form 5 June 2022; Accepted 10 June 2022
2452-199X/© 2022 The Authors. Publishing services by Elsevier B.V. on behalf of KeAi Communications Co. Ltd. This is an open access article under the CC BY-NC-ND license (http://creativecommons.org/licenses/by-nc-nd/4.0/).

chemotherapy or radiotherapy to kill the residue cancer cells [7,8]. The serious side effects induced by the treatment are usually unbearable, especially for patients who have just finished the surgery.

Electrotherapy which kills cancer cells by applying a high-voltage electric pulse that induces the broken of cell membrane, is currently used in clinical practice in the treatment of various cancers [9,10]. As a localized therapy, electrotherapy presents less systemic toxicity compared with chemotherapy and radiotherapy and provides the possibility to alleviate the patient's suffering. However, the requirements of an external electrical device and electrode insertion in the traditional electrotherapy bring obvious limitations, including the potential for infection, restricted mobility of patients, and low patient acceptability [11]. Designing wireless implants that directly apply an electrical stimulus to the around tissues has received extensive research interest. The most widely used strategy is to modify the implant with charged materials, such as piezoelectric materials [12,13], charged polymers [14], or redox materials [15]. Thus, an electric field can spontaneously form around the implant without an external power supply, which simplifies the system and reduces biosafety concerns. However, dynamic regulation cannot be achieved via this strategy; that is, the charged coatings cannot change the stimulus intensity according to real-time demand. Endowing implants with a dynamic electrotherapy ability in a wireless way has gained significant attention. Researchers have realized dynamic regulation of the surface potential of the implants in a stimuli-responsive manner. Through coupling with external stimuli such as mechanical forces [16–18], ultrasonic waves [19–23], electromagnetic waves [24–26], and magnetic fields [27–30], stimuli-responsive implants convert the energy of the external field into electric energy. Stimuli-responsive implants are wireless devices with the advantages of simplicity and convenience. However, the application of stimuli-responsive implants is limited by the penetration depth and possible adverse effects of the external field on human tissues. In addition, most external fields can only be applied artificially and cannot be prompted in response to the varying physiological needs of the human body.

The microenvironment of tumor tissue is different from normal tissues. which is characterized by high reducibility and low pH [31]. A shift of the microenvironment is considered a signal of changing requirements for the physiological function of implants. Compared to materials responsive to external stimuli, materials responsive to endogenous environmental variations are more time-sensitive and have been gaining more attention in constructing stimuli-responsive implants [32]. Although many materials have been reported to exhibit chemical-sensitive properties [33,34], few of them can realize microenvironment-responsive electrotherapy. In addition, designing chemical-sensitive coatings that fulfill the high biocompatibility requirements of implants remains a challenge.

Herein, we constructed Ni–Ti layered double hydroxide (LDH), a p-type semiconductor, films on nitinol alloy and transformed Ni–Ti LDHs into a degenerate state through electrochemical charging treatment. No additional harmful elements were introduced in the film construction process, guaranteeing the biosafety of the film, which has been verified in our previous works [35–37]. As shown in Fig. 1, the degenerate LDH films are in a metastable state. They gradually release charges and recover to a normal state in a physiological environment. The charge release rate is sensitive to the species and concentrations of ions in the microenvironment. Different discharge rates result in different physiological functions, so the behavior of cells around the films can be automatically regulated with the alteration of the microenvironment. *In vitro* and *in vivo* experiments were conducted, verifying that the constructed films can regulate the cell behavior selectively and sequentially. In addition, the transformation between degenerate and nondegenerate states of Ni–Ti LDHs can be regulated cyclically, so the physiological functions of the prepared films can also be artificially adjusted according to demand.

2. Materials and methods

2.1. Preparation of Ni–Ti LDH films on nitinol

Ni–Ti LDH films were grown on the surface of nitinol via a modified method described in our previous work [36]. Briefly, commercially available nitinol (50.8% at.% Ni) wafers with a diameter of 12 mm and a thickness of 1 mm were ultrasonically cleaned in a mixed acidic solution containing 10 vol% hydrofluoric acid (HF, Sinopharm Chemical Reagent, China) and 50 vol% nitric acid (HNO_3, 68%, Sinopharm Chemical Reagent, China). Then, the samples were further ultrasonically cleaned in deionized water and ethanol. The Ni–Ti LDH precursor solution was prepared by mixing 0.715 g nickel chloride hexahydrate ($NiCl_2.6H_2O$, Sinopharm Chemical Reagent, China), 0.125 mL HCl (36%–38%,

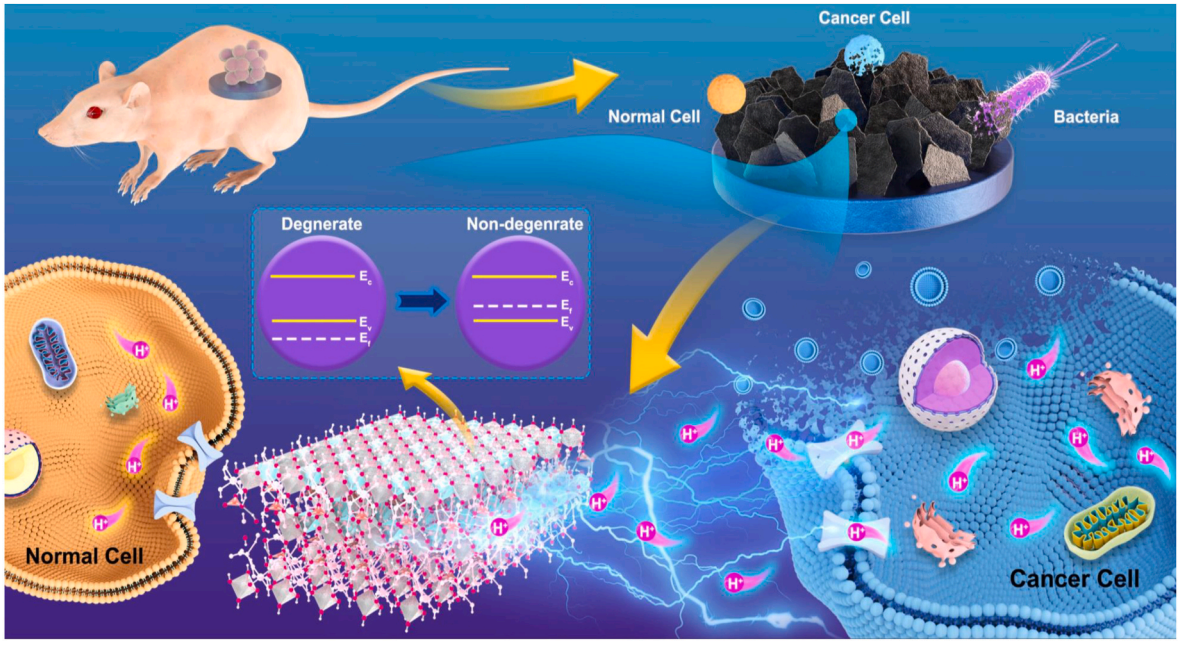

Fig. 1. Schematic illustration of H^+-induced discharging of degenerate LDH films and their selective antitumor and antibacterial effects.

Sinopharm Chemical Reagent, China), 0.125 mL titanium tetrachloride ($TiCl_4$, Sinopharm Chemical Reagent, China) and 3.25 g urea (CH_4N_2O, Aladdin, China) with 1 L ultrapure water. Then, the nitinol wafers were placed in a 200 mL Teflon-lined stainless vessel, and a 65 mL precursor solution was poured into the vessel. The sealed vessel was then placed into a convective oven, heated to 120 °C, and held at this temperature for 24 h. Next, the samples were removed, washed with deionized water, and dried in air.

2.2. Degeneration of Ni–Ti LDH films

Degenerate Ni–Ti LDHs were obtained by electrochemical charging. A two-electrode system was used. The Ni–Ti LDH film-modified nitinol wafer served as the working electrode, a graphite plate served as the counter electrode, and sodium hydroxide (NaOH, Sinopharm Chemical Reagent, China) solution was the electrolyte. The system was connected to a constant current power supply, and the Ni–Ti LDHs were charged under constant currents of −3 mA, 0 mA, 1 mA, and 3 mA for 1 min. The applied voltage was varied with time, owing to the alteration of the conductivity of the film in the charging process. The obtained samples were denoted as LDH(-3 mA), LDH(0 mA), LDH(1 mA), and LDH(3 mA). The applied voltage was varied with time, owing to the alteration of the conductivity of the film in the charging process. Fortunately, the initial voltage was stable since the resistances of the films before charging treatment were almost the same, which was about −1.2 V for LDH(-3 mA), 0 V for LDH(0 mA), 0.8 V for LDH(1 mA), and 1 V for LDH(3 mA). Then, the samples were cleaned with ultrapure water, dried with a dryer, and stored at −20 °C. The degenerate LDHs can recover to a nondegenerate state by discharging LDH(3 mA) with a constant current of −3 mA for 1 min, and conversion between the degenerate state and nondegenerate state can be cyclically realized by charging and discharging treatments.

2.3. Surface characterization

The morphology, chemical composition, crystal phase, and chemical state of the samples were characterized by scanning electron microscope (SEM, Hitachi S4800, Japan), X-ray diffraction (XRD, Rigaku D/max2500, Japan), transmission electron microscope (TEM, Tecnai G2 F20, Japan), and X-ray photoelectron spectroscopy (XPS, RBD upgraded PHI–5000C ESCA system, USA). Samples were directly characterized by all the above technologies according to a previous report [36], except for TEM, for which the films were scraped from the sample surface and mixed with ethanol. A 300 mesh copper grid with a carbon support film was dipped into the obtained suspension, capturing the fragments of the samples for TEM characterization. The stability of the film was investigated by tape test. Briefly, a rectangle of tape was pasted on the surface of the prepared sample. The tape was removed 24 h later, and the sample was observed by SEM. The atomic arrangements of the prepared samples were characterized by X-ray absorption near edge structure (XANES) and X-ray absorption fine structure (XAFS) spectroscopy. The Ni K-edge XANES and XAFS spectra of Ni foil, LDH(-3 mA), LDH(0 mA), LDH(1 mA) and, LDH(3 mA) samples were collected in transmission mode on beamline BL14W1 at Shanghai Synchrotron Radiation Facility, Shanghai Institute of Applied Physics, China. The raw data were processed and fitted by Athena and Artemis software packages. The wavelet transform of the raw data was conducted by MATLAB software packages.

2.4. Theoretical simulation

All the spin theoretical simulations in our work were carried out in the Vienna ab initio Simulation Package (VASP) version 5.4.1. The generalized gradient approximation (GGA) with the Perdew-Burke-Ernzerhof (PBE) functional was employed to evaluate the electron-electron exchange and correlation interactions, while the projector augmented-wave (PAW) method was employed to represent the core-electron (valence electron) interactions. GGA + U calculations were performed with the on-site Coulomb repulsion U term on Ni 3d, and the U_{eff} (U_{eff} = U-J) value was 6.2 eV. The plane-wave basis function was set with a kinetic cutoff energy of 550 eV. The ground-state atomic geometries were optimized by relaxing the force to below 0.02 eV/Å, and the convergence criterion for energy was set to 1.0×10^{-5} eV/cell. Monkhorst-Pack meshes with a size of $3 \times 3 \times 1$ were employed to sample the surface Brillouin zone. The Gaussian method was employed for both the electronic structures and total energy of our models and the stress/force relaxations. To better describe the interactions between molecules, van der Waals (vdw) interactions were included, as described by the DFT-D3 method of Grimme.

2.5. Water contact angle

The water contact angles of various samples were measured by a contact angle meter (SL200b, Solon Information Technology Co., Ltd., China) at 25 °C. Distilled water (2 μL) was added to the sample surface. After 1 min of stabilization, pictures of the water droplet were taken, and the values of the water contact angles were obtained by the tangent method.

2.6. Oxygen production

Samples were immersed in 5 mL water with various pH values, and the oxygen content in the water was measured by a dissolved oxygen microelectrode (Oxy Meter, Unisense, Denmark).

2.7. Charge transfer analysis

The electrochemical properties of the prepared films were acquired by an electrochemical workstation (CHI760C, Chenhua, China). A conventional three-electrode system formed the electrochemical cell, with a saturated calomel electrode (SCE) as the reference electrode, a graphite rod as the counter electrode, and the tested samples as the working electrode. OCP tests were conducted in various electrolytes, including ultrapure water, potassium hydroxide (KOH, 10 μM, Sinopharm Chemical Reagent, China), sodium fluoride (NaF, 10 μM, Sinopharm Chemical Reagent, China), sodium chloride (NaCl, 10 μM, Sinopharm Chemical Reagent, China), potassium chloride (KCl, 10 μM, Sinopharm Chemical Reagent, China) and hydrogen chloride (HCl, 10 μM, Sinopharm Chemical Reagent, China) solutions. The OCP of LDH(3 mA) was also tested in electrolytes with pH values of 4, 6, 7, and 8. The pH value of the electrolyte was adjusted by HCl and KOH solutions.

Linear polarization tests were conducted over the potential range of −1 V–1 V vs. SCE in physiological saline solution (0.9 wt% NaCl, pH = 7), employing a scan rate of 5 mV/min.

Electrochemical impedance spectroscopy (EIS) was conducted at the open-circuit voltage in the frequency range between 10^{-2} Hz and 10^{5} Hz, applying a small perturbation AC signal with an amplitude of 5 mV. The obtained EIS data were analyzed by equivalent circuit modeling using the ZView software package. Gaussian process distribution of relaxation times (DRT) analysis was performed according to the research conducted by J. Liu [38]. The EIS spectra of LDH(3 mA) were obtained every 10 min to investigate the variation in EIS spectra over time, and the results were analyzed by two-dimensional spectral analysis.

The semiconducting properties of different samples were studied by Mott-Schottky (MS) analysis, which was performed at underpotentials ranging from −3 V to 3 V vs. SCE with an interval of 0.05 V at a frequency of 1000 Hz.

The electron transfer between samples and the environment of various samples was tested by scanning electrochemical microscopy (SECM, CHI900D, Chenhua, China). The electrochemical cell was also formed by a three-electrode system with an SCE as the reference electrode, tested samples as the counter electrode, and a platinum wire

electrode as the probe. The probe potential was preset to – 0.5 V and 0.5 V. The probe approach curves (PAC) and the SECM images were acquired following the instructions of the manufacturer.

Current-voltage (I–V) curves were obtained using a semiconductor parameter analyzer (KEITHLEY 5214, USA) both under light irradiation and in the dark. Half of the films were scraped by a rasper to expose the nitinol substrate. As shown in Supplementary Fig. S1 After part of the films have been scraped off, the nitinol substrate would be exposed outside, whose appearance was different from the film, and the differences could be directly distinguished by eyes. In addition, the samples were observed by SEM, it could be found that the films had been scraped off. In the measurement, one probe was placed in contact with the film, while the other probe was placed in direct contact with the substrate with the help of the equipped optical system. Voltages ranging from −3 V to 3 V were applied through the two probes, and the current was recorded.

The surface conductivities of the samples were qualitatively characterized by connecting the samples to a circuit with a miniature bulb, and a voltage of 1 V was applied in the circuit. The conductivity was reflected by the brightness of the bulb; the lower the conductivity was, the brighter the bulb.

2.8. Cell experiments

The cholangiocarcinoma cell line RBE (Cell Bank of the Chinese Academy of Science, China) and the human intrahepatic biliary epithelial cell line HIBEpiC (ScienCell, USA) were used in the *in vitro* experiments since cholangiocarcinoma therapy is a representative application scenario for nitinol implants. The cancer cells were cultured in RPMI 1640 medium supplemented with 10% fetal bovine serum (FBS, Gibco, USA) and 1% antibiotic-antimycotic (Gibco, USA), while normal cells were cultured in epithelial cell medium (EpiCM, ScienCell, USA) supplemented with 2% FBS, 1% antibiotic-antimycotic and 1% epithelial cell growth factor. Both types of cells were cultured in a humidified atmosphere containing 5% CO_2 at 37 °C. Cells were passaged at a ratio of 1:2–1:4 every 2–4 days.

Cell viability. Cells were seeded on samples at a density of 5×10^4 cells/specimen. After culturing for 1, 4, and 7 days, the viabilities of cells cultivated on various samples were tested by alamarBlue™ assay according to the instructions.

Cell morphology observation. Cells were seeded onto sample surfaces at a density of 5×10^4 cells/specimen and cultured for 4 days. Then, the cells were fixed with glutaraldehyde solution (2.5%, Sinopharm Chemical Reagent, China) and dehydrated with a series of ethanol (Sinopharm Chemical Reagent, China) and hexamethyldisiloxane (Sinopharm Chemical Reagent, China) solutions. After drying in air, the morphology of cells on various samples was observed by SEM.

Live/dead cell staining. Cells were seeded on samples at a density of 5×10^4 cells/specimen and cultured for 4 days. Next, cells were stained with a live/dead cell staining kit (BioVision, USA) and observed with confocal laser scanning microscopy (CLSM, Leica SP8, Germany).

JC-1 staining. The apoptosis behavior of cells cultured on different samples was examined by JC-1 staining 4 days after cell seeding (5×10^4 cells/specimen) according to the manufacturer's instructions. JC-1 is a dye that responds to the membrane potential of mitochondria; it shows green fluorescence (wavelength = 520 nm) at low membrane potentials and red fluorescence (wavelength = 596 nm) at high membrane potentials. A membrane potential decrease has been verified to be an important marker of apoptotic cells, so the apoptotic behavior of cells cultured on various samples can be characterized by the fluorescence intensity ratio between red fluorescence and green fluorescence. The stained cells were observed with CLSM for qualitative characterization and dissociated from the samples for quantitative characterization. The stained cells were resuspended in phosphate-buffered saline (PBS, Gibco), and the fluorescence intensity of the cells was measured by a microplate reader (BIO-TEK Synergy H4, USA).

Cell migration. Specimens were immersed in a 1 mL cell culture medium containing no FBS for 2 days. Then, the leach liquor was collected. Cells were seeded into a 24-well plate at a density of 5×10^4 cells/well and cultured for 4 days. Next, some of the cells in the well were scraped by drawing a line across the well with a 100 μL pipette. Then, the culture medium was replaced by the leach liquor of various samples. After culturing for different periods, the cells were stained with fluorescein isothiocyanate (FITC)-phalloidin (Abcam, UK) and 4',6-diamidino-2-phenylindole (DAPI; Abcam, UK) and observed by CLSM. The cell migration was evaluated by counting the number of cells entering the cell-free area.

Real-time quantitative PCR (RT-PCR) analysis. Expression of the apoptosis-related genes Caspase-3 and Bcl-2 was tested by RT-PCR. Cells were cultured on the sample surface at a density of 5×10^4 cells/specimen for 1 day. Total RNA was extracted by TRIzol reagent (Roche, Switzerland) and transformed into cDNA using a Transcriptor First Strand cDNA Synthesis Kit (Roche, Switzerland). RT-PCR was conducted on a LightCycler 480 system (Roche, Switzerland) following the standard procedure reported in previous studies. GAPDH was selected as a reference gene since its expression level in the same type of cell was basically constant. The untreated NiTi sample served as the control group and the expression levels of target genes relative to reference genes in cells cultured on NiTi sample was normalized. The expression levels of target genes in cells cultured on other samples could be determined by the proportion of the expression levels of standardized target genes/GADPH value of cells cultured on NiTi sample. The primer sequences of *Caspase-3* and *Bcl-2* used in this study are listed in Supplementary Table S1.

2.9. In vitro antibacterial experiment

Bacterial culture. *Staphylococcus aureus* (*S. aureus*), *Escherichia coli* (*E. coli*), and *Pseudomonas aeruginosa* (*P. aeruginosa*) were chosen to evaluate the antibacterial properties of the samples. *S. aureus* cells were cultured in nutrient broth (NB, Sigma, USA) or on NB agar plates. E. coli and *P. aeruginosa* were cultured in Luria–Bertani (LB, Sigma, USA) broth or on LB agar plates. Before bacterial culture, all samples sterilized with 75% ethanol solution were placed in 24-well bacterial culture plates. Then, 500 μL bacterial suspension with a concentration of 10^6 CFU/mL was added to each well and incubated in a 37 °C incubator for various periods.

Colony counting. The colony counting method was used to test the antibacterial ability of various samples. After 24 h of cultivation, samples were placed in centrifuge tubes with 4 mL 0.9% NaCl solution and vigorously shaken to make the bacteria fall off. The concentration of the bacterial solutions was diluted 100 times with 0.9% NaCl solution. Diluted bacterial solutions were evenly daubed on bacterial culture plates (100 μL/well). All culture plates were placed in a 37 °C incubator upside down for 18 h and then visualized by a gel imaging system (FlourChem M, ProteinSimple, USA). The number of colonies was counted.

Live/dead bacterial staining. After 24 h of cultivation, the bacteria-inoculated samples were rinsed twice with sterilized PBS solution and stained with Live/Dead® BaclightTM Bacterial Viability Kits (L13152, BioVision, USA) for 15 min at 37 °C. CLSM was used to observe the distribution of live/dead bacteria on the sample surfaces.

2.10. In vivo experiment

The animal experiments were approved by the animal ethics committee of Guangdong provincial people's hospital (approval number: KY-Q-2021-236-01).

Although different kinds of bacteria are found in the infection sites, the most commonly isolated microorganisms are *S. aureus,* which account for 33.8% of medical device infections [39]. Therefore, we chose *S. aureus* to develop *in vivo* bacterial infection model. Samples were

immersed in 500 μL *S. aureus* suspension (concentration: 10^8 CFU/mL). The bacteria-contaminated sample was immediately implanted into a subcutaneous pocket made on the back of a BALB/c mouse and harvested 1 day later. The mice were sacrificed, and the skin contacting the sample surface was dissected and embedded in paraffin. Histological cross-sections of the tissues were stained with H&E. Residual bacteria on the harvested samples were collected and evenly daubed on bacterial culture plates (100 μL/well). All culture plates were placed in a 37 °C incubator upside down for 18 h and then visualized by a gel imaging system.

To develop an *in vivo* tumor model, 100 μL cancer cell suspension at a density of 2×10^6 cells/mL was injected into the underarm of BALB/c nude mice. One week later, the tumor-bearing mice were anesthetized with pentobarbital sodium. One subcutaneous pocket was made at the tumor site, and the nitinol substrate with as-made film on it was implanted into the pocket, contacting the tumor directly. The incision was then sutured. The tumor size was measured by a caliper, and its volume was calculated according to previous research [36]. The mice were sacrificed two weeks after sample implantation. Blood was collected from each mouse for routine analysis and blood biochemical

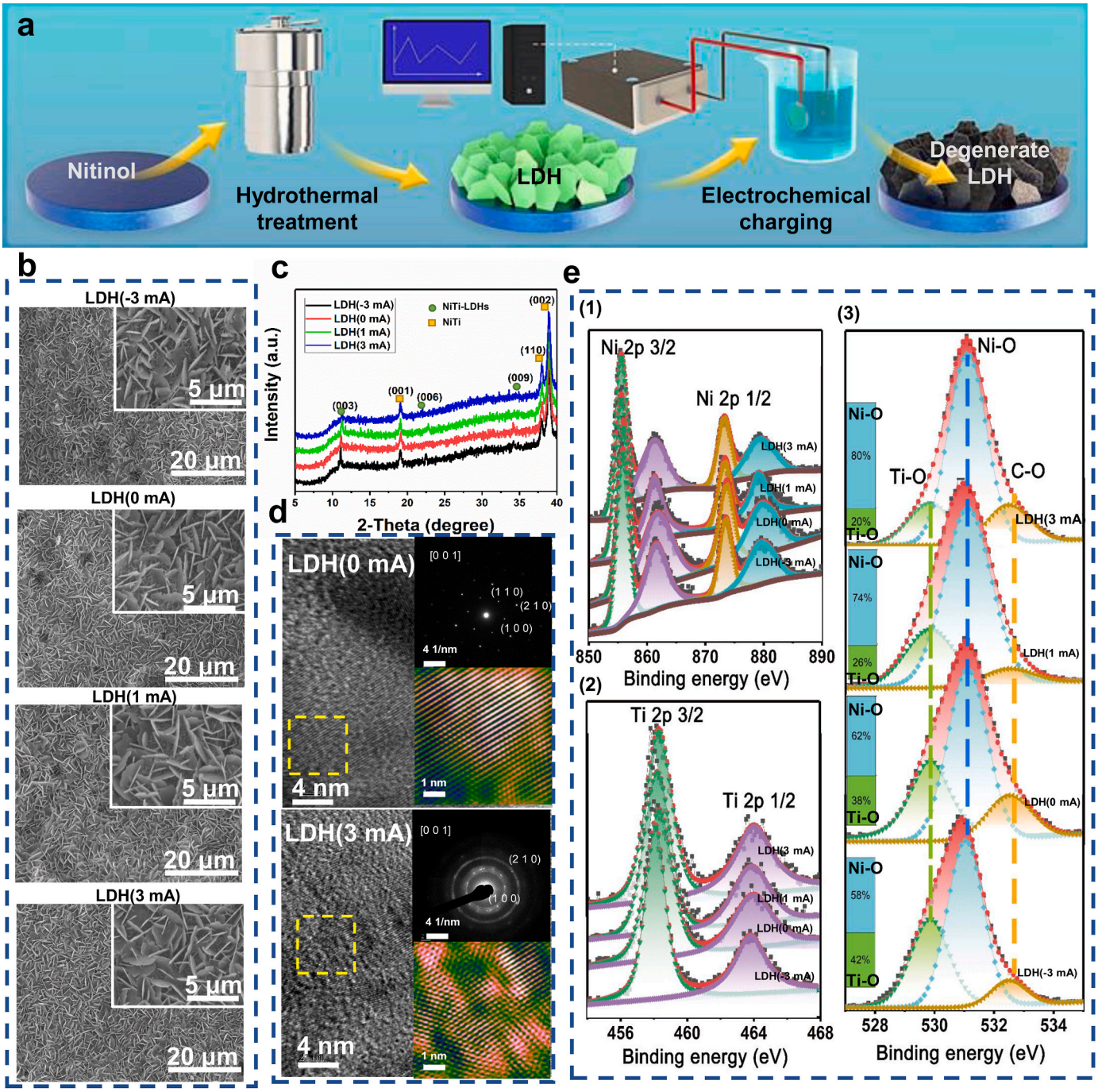

Fig. 2. Preparation and characterization of degenerate LDH films on nitinol substrates. (a) Schematic diagram depicting the preparation process of degenerate LDH films. (b) SEM images of LDH(-3 mA), LDH(0 mA), LDH(1 mA) and LDH(3 mA) samples. (c) XRD patterns of LDH(-3 mA), LDH(0 mA), LDH(1 mA) and LDH(3 mA) samples. (d) HRTEM images of LDH(0 mA) and LDH(3 mA) samples. The insert image at the top right shows the SAED pattern, and the insert image at the bottom right shows the magnified image of the area marked by the yellow dotted box. (e) High-resolution XPS spectra of Ni (e−1), Ti (e−2), and O (e−3) acquired from LDH (-3 mA), LDH(0 mA), LDH(1 mA) and LDH(3 mA) samples.

index tests. Since all the indices can be directly compared to the existing data of healthy mice, we didn't include the group without any treatment. Tumors and organs, including the heart, lung, spleen, kidney, and lung, were dissected from the body and embedded in paraffin. Histological cross-sections of the tumors and the abovementioned organs were stained with H&E. The tumors were also stained by a TUNEL kit (Roche, Switzerland). Images were obtained with a fluorescence microscope.

2.11. Data analysis

Experiments were conducted in triplicate. Statistical analyses were performed with the GraphPad Prism 5 statistical software package. Data were expressed as the mean ± standard deviation. Statistically significant differences (p) were analyzed by one-way analysis of variance and Tukey's multiple comparison tests and marked in the graphs with the symbols "*" ($p < 0.05$), "**" ($p < 0.01$), and "***" ($p < 0.001$).

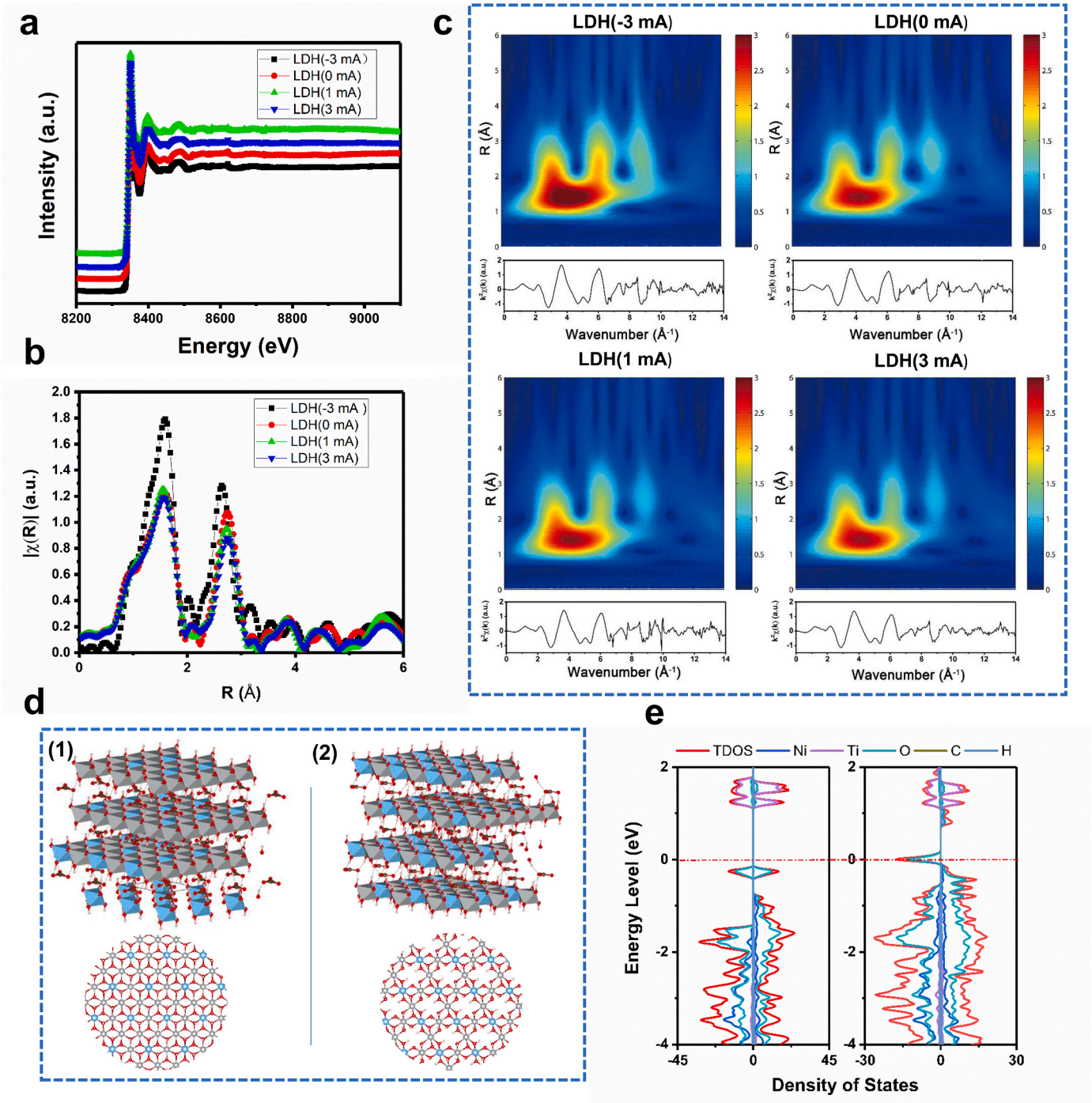

Fig. 3. Analysis and calculation of the coordination of Ni in degenerate LDH films. (a) Normalized XANES spectra at the Ni K-edge of LDH(-3 mA), LDH(0 mA), LDH (1 mA) and LDH(3 mA) samples. k2-weighted Fourier transform spectra from EXAFS spectra of LDH(-3 mA), LDH(0 mA), LDH(1 mA) and LDH(3 mA) samples. (c) Ni K-edge EXAFS spectra and modulus of their Morlet wavelet transform for LDH(-3 mA), LDH(0 mA), LDH(1 mA) and LDH(3 mA) samples. (d) Supercell models for chemometric NiTi LDHs (d-1) and NiTi LDHs with Ni vacancies (d-2), in which the gray ball represents Ni, the blue ball represents Ti, the red ball represents O, the pink ball represents H, and the brown ball represents C. (e) Total density of states of chemometric LDHs and LDHs with Ni vacancies.

3. Results and discussion

3.1. Construction and characterization of the degenerate LDH films

Fig. 2a shows a schematic diagram of the process to construct degenerate Ni–Ti LDH films, which mainly includes two major processes: hydrothermal treatment of nitinol plate to growth LDH films, electrochemical charging of the LDH films via a constant current power supply, rendering LDH films transform to degenerate state. All samples presented similar platelet-like topography (Fig. 2b). The width and length of the platelets were approximately 2 μm which is similar to the morphology of Ni–Ti LDH films constructed in previous reports [36]. The thickness of the films on all the samples was kept constant (Supplementary Fig. S2), suggesting charging treatment did not affect the growth process of the films. The results of the tape test show the film still presented intact plate morphology and was not stuck out by the tape, indicating good stability of the obtained samples (Supplementary Fig. S3). XRD patterns are presented in Fig. 2c. All samples showed peaks centered at 11.2° and 22.4°, which can be indexed to the characteristic (0 0 3) and (0 0 6) crystal planes of Ni–Ti LDHs [40,41]. With increasing charging current, the peaks corresponding to Ni–Ti LDHs gradually weakened and broadened, indicating that the electrochemical charging process reduced the crystallinity of the prepared films. High-resolution transmission electron microscopy (HRTEM) and selected area electron diffraction (SAED) images (Fig. 2d) confirmed the good crystallinity of the prepared LDH films. No obvious lattice orientation alteration could be found in the LDH(0 mA) sample. In addition, the SAED image of the LDH(0 mA) sample displayed clear diffraction spots that could be indexed to the (1 0 0), (2 1 0) and (1 1 0) crystallographic planes, indicating that the constructed LDH nanoplates were monocrystals. Small grains with varied orientations appeared in the HRTEM images of the LDH(3 mA) sample, and the diffraction spots transformed into diffraction rings, suggesting that charging treatment changed the LDH films to polycrystals. XPS measurements showed that all the prepared films were composed of C, O, Ti, and Ni elements (Supplementary Fig. S4). The Ni 2p1/2 and Ni 2p3/2 peaks centered at 874 eV and 857 eV corresponding to the binding energies of Ni^{2+} in Ni–OH (Figs. 2e-1). Ti 2p1/2 (464 eV) and Ti 2p3/2 (485 eV) peaks could be recognized for all the prepared films (Fig. 2e-), which can be ascribed to the existence of Ti^{4+}. The above results further verified the successful construction of Ni–Ti LDHs and indicated no obvious valence variation in Ni–Ti LDHs after electrochemical charging treatment. As shown in Figs. 2e-3, the O1 s peak could be divided into three peaks centered at 532.9, 531.0, and 529.9 eV, corresponding to the binding energy of O in *C*–O, Ni–OH, and Ti–OH bonds, respectively. The inset picture shows the content percentages of Ni–OH and Ti–OH in various samples. With increasing charging current, the Ni–OH content in the film decreased, while the Ti–OH content increased.

The coordination of Ni in different samples determined their physical and chemical properties directly, which could be characterized by XANES and XAFS. XANES is element-specific and highly sensitive to the local structure of the absorbing atoms. Extended XAFS (EXAFS) can determine the coordination profiles of the absorbing atoms. The XANES spectra of LDH(-3 mA), LDH(0 mA), LDH(1 mA), and LDH(3 mA) share similar *K*-edge positions (Fig. 3a), indicating that the chemical valences of Ni in different samples are the same, which is following the XPS results (Figs. 2e-1). Fig. 3b shows the Fourier transforms of the EXAFS spectra of Ni for different samples. Two peaks appeared in all samples, and the peak positions were very similar, located at 1.8 and 2.3 Å, corresponding to the bond lengths of the first coordination layer and second coordination layer. Wavelet transform of the EXAFS spectra was performed to confirm the coordination atoms around Ni, and the results are shown in Fig. 3c. Different coordination elements present different k-space oscillation modes. For lighter elements, the strongest oscillation in k-space appears at a lower wavenumber, while for heavier elements, the strongest oscillation in k-space appears at a higher wavenumber. Four peaks appeared in the wavelet transformed image, located at (1.5 Å, 4 $Å^{-1}$), (2.3 Å, 4 $Å^{-1}$), (2.3 Å, 6 $Å^{-1}$), and (2.3 Å, 8 $Å^{-1}$), indicating that only one element existed in the first coordination layer but three different elements existed in the second coordination layer. The film was verified to only contain four elements: C, O, Ti, and Ni. The obtained peaks could be indexed to confirmed elements according to their molecular weight. The nearest coordination atom of Ni in the film was O (1.5 Å, 4 $Å^{-1}$), while the three elements O (2.3 Å, 4 $Å^{-1}$), Ti (2.3 Å, 6 $Å^{-1}$), and Ni (2.3 Å, 8 $Å^{-1}$) existed at the second-nearest sites, which is well consistent with the atom arrangement in the Ni–Ti LDH crystal structure. Note that the intensity of the peak corresponding to the coordinated Ni decreased with increasing charging current, suggesting that the charging treatment reduced the Ni content in the Ni–Ti LDH film, following the XPS results (Figs. 2e-3). EXAFS fitting was conducted to obtain the detailed structural parameters of various samples (Supplementary Fig. S5, Supplementary Fig. S6). The fitting data are shown in Supplementary Table S2. The coordination numbers of Ni–O in all samples were similar, approximately 6, while the coordination number of Ni–Ni decreased from 7.59 to 5.18 with increasing charging current, further verifying that electrochemical charging brought Ni out of the prepared film and resulted in the formation of Ni vacancies.

Based on the above material characterization results, two types of crystal structures were built to calcu5late the band structure of Ni–Ti LDH before and after electrochemical charging (Fig. 3d). The difference between the two structures lies in the Ni content: some of the Ni atoms in the original Ni–Ti LDH structure were deleted in the crystal model of the charged samples. The calculated band structures, partial density of states, and total density of states are shown in Supplementary Fig. S7, Supplementary Fig. S8, and Fig. 3e, respectively. The chemometric Ni–Ti LDH exhibit a typical band structure of a semiconductor with the Fermi level, which is calculated to be 1.42 eV, located in the forbidden band. The valence band is mainly composed of O 2p orbitals, while the conduction band is mainly composed of Ti 3d orbitals. The valence band maximum of chemometric Ni–Ti LDH locates at 0.039 eV below the Fermi level, while its conduction band bottom locates at 1.020 eV above the Fermi level. The Fermi level is closer to the valence band compared to the conduction band, which is the typical characteristic of p-type semiconductors, and is consistent with the bandgap of traditional LDH materials [42]. The Fermi level of LDH films containing Ni vacancies, which is calculated to be 0.46 eV moves to the valence band, indicating that reducing the Ni content in Ni–Ti LDHs transforms the samples into a degenerate state; hence, the carrier density in the Ni-deficient LDH films increases and the conductivity accordingly increases. Based on the above results, the chemometric LDH(-3 mA) and LDH(0 mA) samples should be in nondegenerate states, and the Ni-deficient LDH(1 mA) and LDH(3 mA) samples should be in degenerate states.

To verify the calculation results, the conductivities of the constructed films were qualitatively characterized by connecting the samples in a circuit containing a miniature bulb (Fig. 4a, Supplementary Fig. S9). A voltage of 1 V was applied in the circuit, and the lightness of the bulb was inversely correlated with the resistance of the films. The brightness and current flowing in the circuit showed the following trend: LDH(3 mA) > LDH(1 mA) > LDH(-3 mA) > LDH(0 mA). The results illustrated that electrochemical charging increased the conductivity of the LDH films and that charging the samples with a positive current was more effective in decreasing the film resistance. I–V curve measurements were conducted to quantitatively test the electrical property variation of different samples. As shown in the inset image of Fig. 4b, the measurement was conducted with a two-probe system. Part of the film was scraped from the sample, one probe was directly contacted to the exposed substrate, and the other probe was contacted to the unspoiled film. The slopes of the I–V curves for various samples increased with the electrochemical charging current. The slopes of the LDH(-3 mA) and LDH(0 mA) samples were close to zero ($\approx 10^{-11}$), showing their high resistance characteristics. The curve slope increased by three orders of magnitude for LDH(1 mA) and four orders of magnitude for LDH(3 mA),

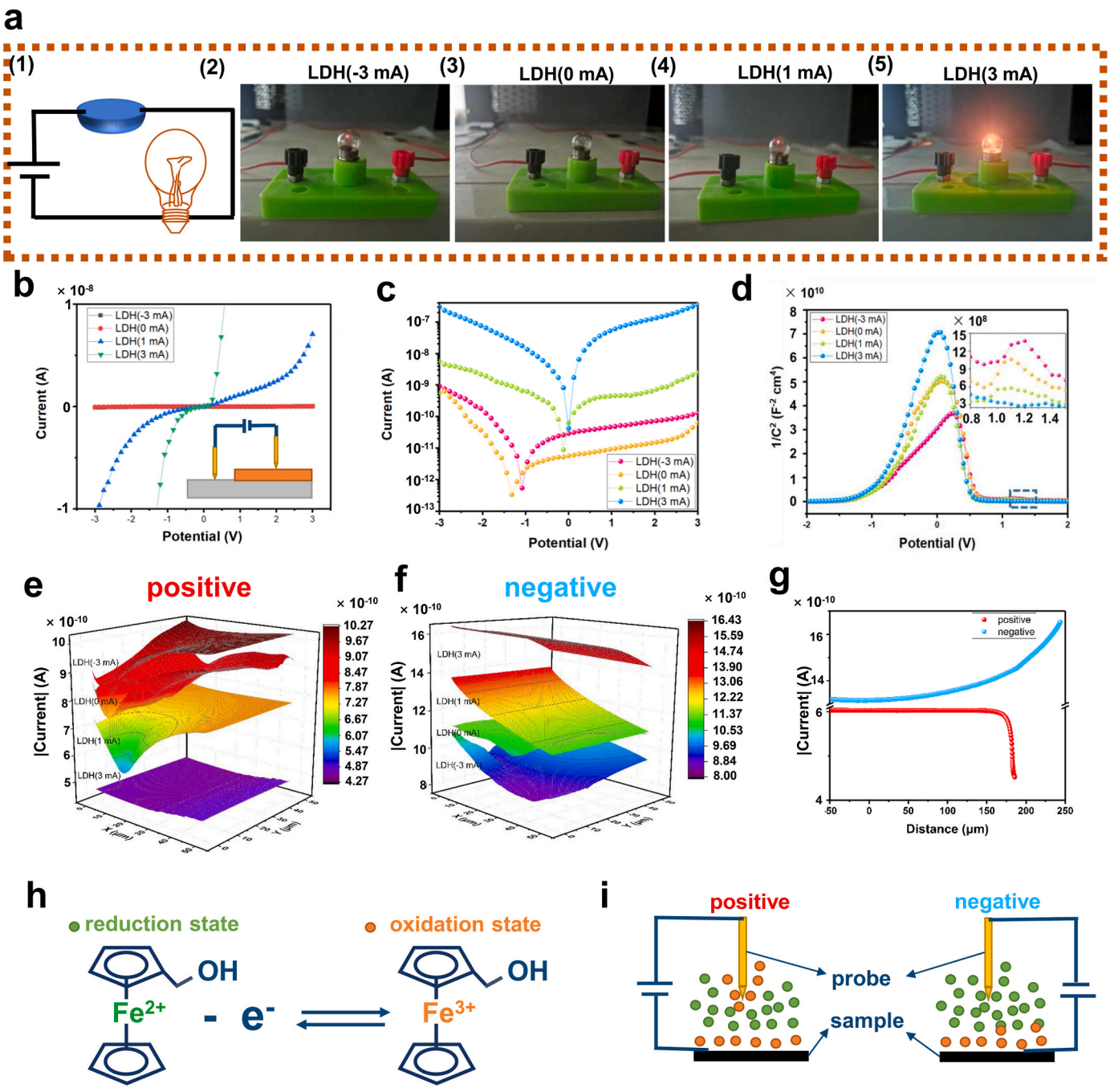

Fig. 4. Characterization of the conductivity and charge carriers in degenerate LDH films. (a) Photos showing the brightness of a small bulb in a constant voltage circuit (a-1) connected to LDH(-3 mA) (a-2), LDH(0 mA) (a-3), LDH(1 mA) (a-4) and LDH(3 mA) (a-5) samples. (b) I–V curves of LDH(-3 mA), LDH(0 mA), LDH(1 mA) and LDH(3 mA) samples measured in the dark. The inset image shows the test circuit. (c) I–V curves of LDH(-3 mA), LDH(0 mA), LDH(1 mA) and LDH(3 mA) samples. The curves were obtained under light, and the y-coordinate was plotted in logarithmic form. (d) MS curves of LDH(-3 mA), LDH(0 mA), LDH(1 mA) and LDH (3 mA) samples. (e) SECM images of LDH(-3 mA), LDH(0 mA), LDH(1 mA) and LDH(3 mA) samples when the applied voltage was 0.5 V. (f) SECM images of LDH(0 mA), LDH(1 mA) and LDH(3 mA) samples when the applied voltage was −0.5 V. (g) PACs of LDH(3 mA) samples with a positive or negative applied voltage. (h) Illustration of the redox transformation between ferrocene and ferrocenium in the electrolyte in SECM characterization. (i) Schematic diagram depicting the distribution of ferrocene/ferrocenium in the electrolyte when the voltage applied on the probe is positive or negative.

indicating the significant conductivity improvement of the LDH(1 mA) and LDH(3 mA) samples. The change in the electronic band structure also affects the contact modes between the nitinol substrate and the prepared film. To investigate the contact modes, the I–V curves were plotted in logarithmic coordinates. As shown in Supplementary Fig. S10, the lowest points in the I–V curves of LDH(1 mA) and LDH(3 mA) were located at a potential of 0 V, indicating the formation of ohmic contact, while those of LDH(-3 mA) and LDH(0 mA) deviated from the zero point, which is the characteristic feature of Schottky contact. The deviation became more obvious for LDH(-1 mV) and LDH(0 mV) when the measurement was conducted under light (Fig. 4c) owing to the existence of Schottky barriers that induced a self-built electric field at the interface between the substrate and the film, widely known as the photoelectric effect. In contrast, the lowest point in the I–V curves of LDH(1 mA) and LDH(3 mA) was still located at 0 V when these samples were exposed to light, verifying that no energy barrier existed at the interface between

the film and the nitinol substrate. The above results were consistent with the calculation results, showing that the chemometric LDH(-3 mA) and LDH(0 mA) samples were in nondegenerate states with large electrical resistance, while the Ni-deficient LDH(1 mA) and LDH(3 mA) samples were in conductive degenerate states.

The types and density of charge carriers in various samples were tested by MS curves (Fig. 4d). In the MS plots, a positive slope indicates the existence of electrons, while a negative slope indicates the existence of holes. The charge carrier density can be calculated from the value of the slope. The quantitative results are presented in Supplementary Table S3. Both electrons and holes can be found in the films, but the density of holes ($>10^{20}/cm^3$) is obviously higher than that of electrons ($>10^{17}/cm^3$), confirming the p-type semiconductor nature of LDH films. The detected electrons may stem from the titania (TiO_2) layer formed in the construction of LDH films. TiO_2 is an n-type semiconductor [43,44] that spontaneously grows beneath LDH films during hydrothermal treatment [45]. The electrochemical charging process had no obvious effect on the electron density but could effectively increase the hole density. In particular, the hole density in LDH(3 mV) reached $2.35 \times 10^{22}/cm^3$, which is comparable to the charge carrier density in conductors, verifying that the LDH films were transformed into a degenerate state.

The major charge carriers in the degenerate LDH films are holes, not electrons, which can be further verified by SECM characterization. When a positive voltage was applied to the probe, the measured currents showed the following trend: LDH(-3 mA) > LDH(0 mA) > LDH(1 mA) > LDH(3 mA) (Fig. 4e). When the applied voltage was negative, the reverse trend was obtained (Fig. 4f). In addition, the PAC results indicated different conductive characteristics of the degenerate LDH(3 mA) samples when applying a positive or negative voltage to the probe (Fig. 4g). When applying a positive voltage, the measured current decreased with the approach of the probe to the sample surface, indicating that the tested samples presented high electrical resistance. When the applied voltage was negative, the measured current increased with the approach of the probe and sample, showing the characteristics of a conductor. In contrast, the LDH films in the nondegenerate state maintained their high resistance characteristics regardless of whether the applied voltage was negative or positive (Supplementary Fig. S11). This interesting phenomenon resulted from the charge carriers in the degenerate LDH films being positively charged holes, and the holes in the films presented high oxidation ability. In the SECM tests, hydroxyl ferrocene, a redox agent, existed in the electrolyte. The magnitude of the measured current was determined by the redox reaction rate of ferrocene/ferrocenium (Fig. 4h). When the applied voltage was positive, the redox reaction proceeded forward, and the reaction rate was determined by the concentration of ferrocene. However, the holes in degenerate LDH films oxidized ferrocene and decreased its concentration, thus lowering the reaction rate and reducing the measured current. The concentration of ferrocene decreased with the approach of the probe to the sample surface, leading to the decreased current shown in the PAC measurement. In contrast, when the applied voltage was negative, the magnitude of the measured current was determined by the concentration of ferrocenium, which is the oxidized counterpart of ferrocene. The holes in the degenerate LDH films increased the concentration of ferrocenium in the electrolyte, so a higher current could be detected from the degenerate LDH films.

Based on the above analysis, degenerate LDH films (LDH(1 mA) and LDH(3 mA) samples) with high conductivity were successfully constructed on the nitinol substrates, and the major charge carriers in the films are positively charged holes. The appearance of holes in the degenerate LDH films can be ascribed to the generation of Ni vacancies in the charging treatment. The Ni^{2+} in LDHs, as p-type semiconductors, present much higher mobility than O^{2-}. When a positive voltage was applied to the samples, the positively charged Ni moved along the electric field and entered the electrolyte, leaving Ni vacancies (V_{Ni}'') in the films, so Ni deficiency was found in the degenerate LDH films. Positively charged holes were generated along with Ni vacancies (Equation (1)), thus increasing the concentration of charge carriers in the films and transforming the films into a conductive degenerate state. It should be noted that LDH(-3 mA) samples also presented high conductivity than LDH(0 mA), which may stem from that charging LDH with negative voltage increase the electron density in the film.

$$V_{Ni}^{Ni} = V_{Ni}'' + 2h^{\bullet} \quad (1)$$

3.2. Hole transfer between degenerate LDH films and the environment

When the samples are immersed in a physiological environment, holes stored in the degenerate LDH films can flow out, and the exchange of charges between the samples and the environment is an electrochemical reaction in nature, which can be characterized by electrochemical measurements. The polarization curves presented in Fig. 5a show an increased self-corrosion voltage of the degenerate LDH films, which can be ascribed to the accumulation of positively charged holes in the degenerate LDH films. According to the Nyquist curves (Fig. 5b) acquired from EIS tests, the radii of the impedance arcs showed the following trend: LDH(0 mA) > LDH(-3 mA) > LDH(1 mA) > LDH(3 mA), which is following the conductivity test results, illustrating higher electron transfer efficiency in the degenerate LDH films. The EIS Bode curves further confirmed the reduced impedance of the degenerate LDH films. As shown in Fig. 5c, the impedance of the LDH(3 mA) sample in the low-frequency region was only one-tenth that of LDH(0 mA). In the phase angle plot (Fig. 5d), two peaks centered at approximately 0.1 Hz and 1000 Hz could be detected from the nondegenerate LDH(-1 mA) and LDH(0 mA) samples, while only one peak centered at approximately 0.1 Hz could be found in the degenerate LDH(1 mA) and LDH(3 mA) samples. The peak located in the high-frequency region (1000 Hz) corresponded to the quick responsive electron transfer process, while the slow mass transfer (namely, the ion diffusion process) corresponded to the peak in the low-frequency region (0.1 Hz). Based on the above results, an equivalent circuit model (ECM) with two capacitive elements was used to fit the EIS data of LDH films in the nondegenerate state (LDH(-1 mA) and LDH(0 mA)), while an ECM with three capacitive elements was used to fit the EIS data of LDH films in the degenerate state (LDH(1 mA) and LDH(3 mA)). The two types of ECMs are shown in Fig. 5e, and the parameters acquired from the ECM fitting are presented in Supplementary Table S4. In the ECM of LDH(-3 mA) and LDH(0 mA), $\boldsymbol{R_s}$ represents the resistance of the electrolyte solution, and $\boldsymbol{R_{ct\text{-}1}}$ represents the charge transfer resistance between the LDH film and the electrolyte, and ***CPT-1*** represents the capacitive constant phase element of the LDH film. Note that the LDH film can hardly completely cover the substrate, and the electrolyte can directly contact the nitinol through pores in the LDH film; thus, additional elements need to be introduced into the ECM to simulate the charge transfer process between the substrate and electrolyte. As shown in Figs. 5e-2, $\boldsymbol{R_p}$ represents the resistance of the electrolyte in the pores of the film, and $\boldsymbol{R_{ct\text{-}2}}$ and ***CPT-2*** represent the charge transfer resistance and constant phase element at the interface between the substrate and electrolyte. The dynamics of the electrochemical reaction are determined by charge transfer and mass transfer processes. With regard to the nondegenerate LDH(-3 mA) and LDH(0 mA) samples, the charge transfer resistance is very large ($\boldsymbol{R_{ct\text{-}1}} = 7.3 \times 10^9$ and 2.01×10^6 for LDH(-3 mA) and LDH(0 mA), respectively). Therefore, charge transfer between the LDH films and electrolyte has difficulty proceeding and becomes the rate-limiting step. In contrast, a large number of holes exist in the degenerate LDH(1 mA) and LDH(3 mA) samples, so charge transfer is easier in these films, which can be verified by the lower charge transfer resistance ($\sim 10^4$ Ω). Thus, mass transfer, namely, the ion diffusion process, becomes the critical step in determining the electrochemical reaction rate. Therefore, an additional diffusion-related impedance $\boldsymbol{Z_d}$ appears in the ECM of the degenerate

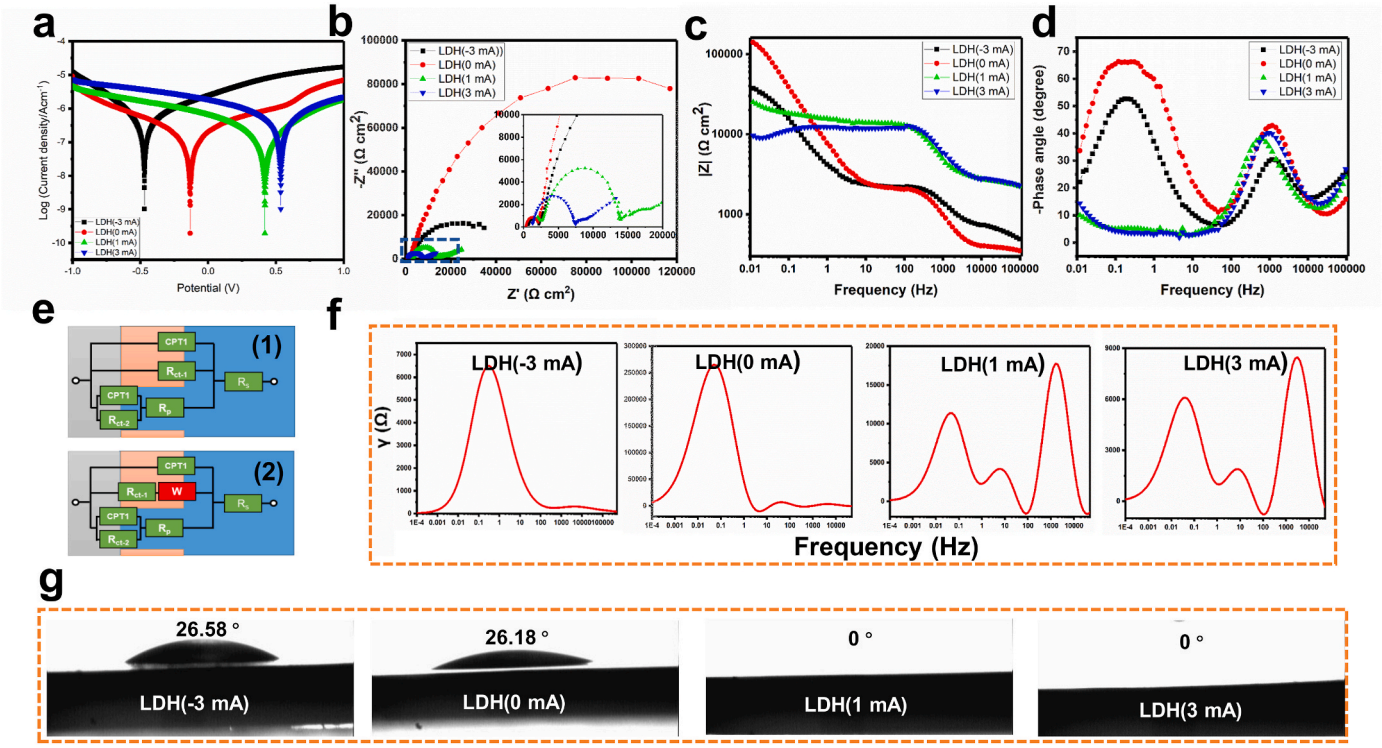

Fig. 5. Hole transfer in the degenerate LDH films. (a) Polarization curves of LDH(-3 mA), LDH(0 mA), LDH(1 mA) and LDH(3 mA) samples. EIS Nyquist plots of LDH (-3 mA), LDH(0 mA), LDH(1 mA) and LDH(3 mA) samples. The inset image shows a magnified image of the area marked by the blue dotted box. (c) Impedance of LDH(-3 mA), LDH(0 mA), LDH(1 mA) and LDH(3 mA) samples acquired by EIS measurements. (d) Phase angle of LDH(-3 mA), LDH(0 mA), LDH(1 mA) and LDH(3 mA) samples acquired by EIS measurements. (e) Equivalent electrical circuits used for the fitting of EIS data of the LDH films in the nondegenerate state (e−1) and degenerate state (e−2). (f) DRT spectra of LDH(-3 mA), LDH(0 mA), LDH(1 mA) and LDH(3 mA) samples. (g) Water contact angles of LDH(-3 mA), LDH(0 mA), LDH (1 mA) and LDH(3 mA) samples.

LDH(1 mA) and LDH(3 mA) samples. According to the EIS test results, charges in the degenerate LDH films can be more easily transported to the outside compared to their counterparts in the nondegenerate films.

Recognizing all the electrochemical processes from the original EIS data is difficult, so a previously reported DRT method was applied to interpret the EIS data in depth [38]. The obtained DRT spectra are shown in Fig. 5f. A strong peak centered at approximately 0.1 Hz (ion diffusion process) and a weak peak at 1000 Hz (electron transfer process) could be observed in the DRT spectra, indicating that the ion diffusion process was easier than electron transfer and the electron transfer process was the rate-determining step for LDH(-1 mA) samples, consistent with the ECM fitting results. A new peak centered at approximately 10 Hz appeared in the DRT spectra of LDH(0 mA), which can be ascribed to the hole diffusion process in the films. However, the strongest peak in the DRT spectra of the LDH(0 mA) sample still appeared at 0.1 Hz, and the weakest peak remained at 1000 Hz, so the rate-determining step for LDH(0 mA) was also the electron transfer process. The situation was different for the degenerate LDH(1 mA) and LDH(3 mA) samples. The peak corresponding to the electron transfer process (1000 Hz) became the strongest peak, whereas the intensity of the peak located at 0.1 Hz decreased, suggesting that electron transfer was the easiest step in the whole electrochemical reaction, further confirming the high charge carrier density in the degenerate LDH films. The weakest peak was located at approximately 10 Hz, showing that the hole diffusion process is the rate-determining process in the degenerate films.

Based on the DRT analysis, the charge transfer between the degenerate LDH films and the environment included three processes, namely, hole diffusion, ion diffusion, and electron transfer, among which hole diffusion was the rate-determining step. Holes that move to the material surface have been reported to possess high activity, and they could react with lattice O, resulting in the production of O_2 and leaving O vacancies in the film [46] (Equation (2)).

$$2O_O + 2h^{\bullet} = O_2 \uparrow + V_O^{\bullet\bullet} \quad (2)$$

We measured the O_2 content in the leach liquor of various samples, and the results (Supplementary Fig. S12) showed that the degenerate LDH(3 mA) sample presented the highest ability to produce O_2 when immersed in ultrapure water, followed by the LDH(1 mA) sample. In contrast, the LDH(0 mA) and LDH(-3 mA) samples, which were in the nondegenerate state, did not produce any O_2. The water contact angle of different samples was measured, and the results are shown in Fig. 5g. LDH(-3 mA) and LDH(0 mA) presented water contact angles of approximately 26°, while the LDH(1 mA) and LDH(3 mA) samples possessed super hydrophilicity, with water contact angles of 0° (Supplementary Video S1). The super hydrophilicity of the degenerate LDH films were resulted from the O vacancies generated along with O_2 production. Water molecules in the air can dissociate and adsorb to the O vacancies to form surface hydroxyl groups, which further adsorb the water in the air to make the surface hydrophilic [47]. The above results were consistent with Equation (2), confirming the high reactivity of holes in the degenerate LDH films and showing that the holes in the films can gradually transfer to the outside and be exhausted when the films are immersed in a physiological environment.

Supplementary data related to this article can be found at https://doi.org/10.1016/j.bioactmat.2022.06.004.

3.3. Hole transfer-induced transformation of degenerate LDH films into a nondegenerate state

The gradual hole transfer can be further verified by open-circuit potential (OCP) tests. As shown in Fig. 6a, in the initial phase of

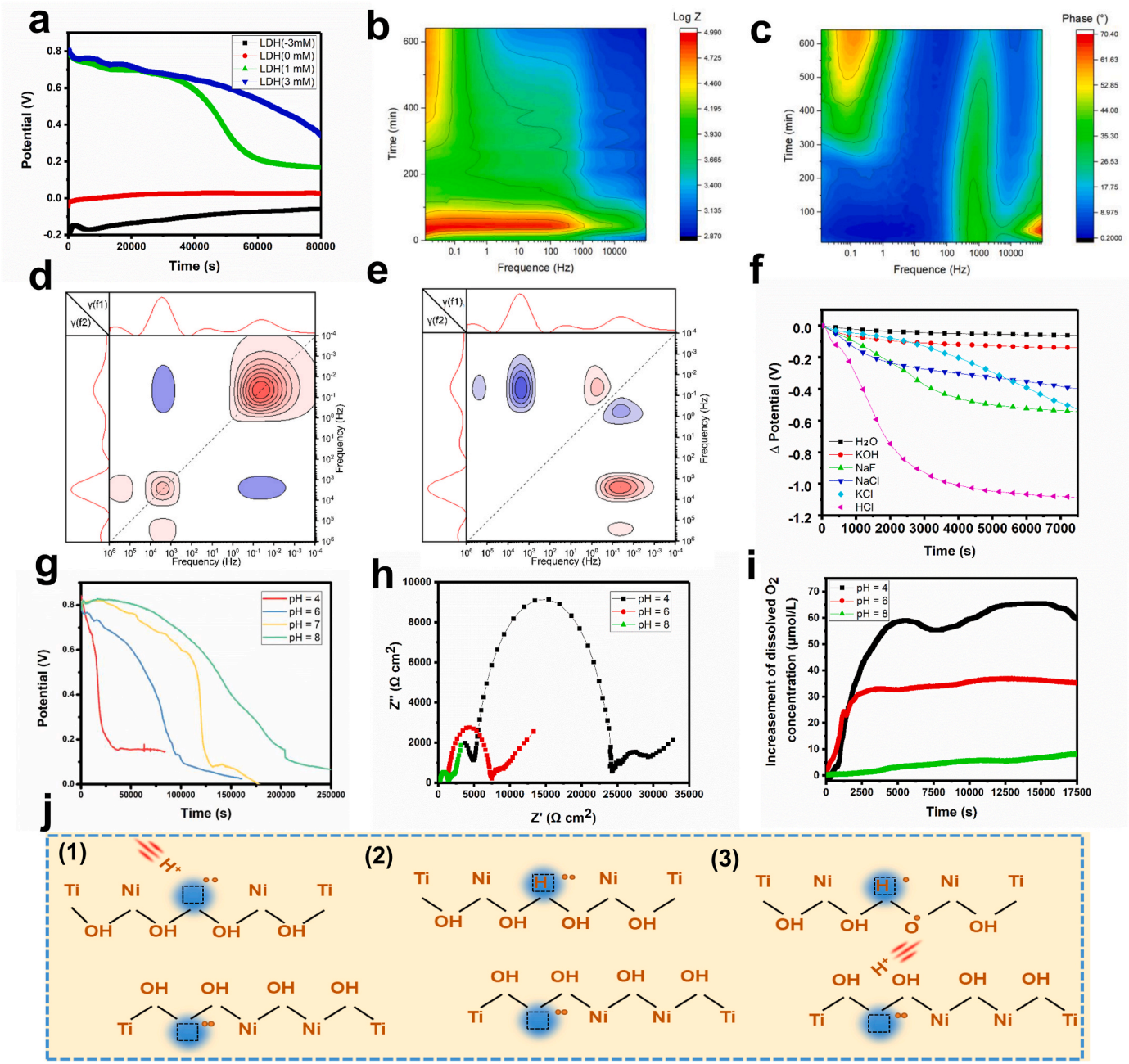

Fig. 6. H^+-responsive hole release and transformation from the degenerate state to the nondegenerate state of degenerate LDH films. (a) OCP curves of LDH(-3 mA), LDH(0 mA), LDH(1 mA) and LDH(3 mA) samples. (b) Evolution of the impedance of the LDH(3 mA) sample acquired by sequential EIS measurements. (c) Evolution of the phase angle of the LDH(3 mA) sample acquired by sequential EIS measurements. (d) Two-dimensional DRT synchronous correlation spectrum of the LDH(3 mA) sample. (e) Two-dimensional DRT asynchronous correlation spectrum of the LDH(3 mA) sample. (f) OCP alteration of LDH(3 mA) samples immersed in electrolytes containing different types of ions. (g) OCP alteration of LDH(3 mA) samples immersed in electrolytes with different pH values. (h) EIS Nyquist plots of LDH(3 mA) immersed in electrolytes with different pH values. (i) Amounts of dissolved O_2 in the solutions with different pH values in which LDH(3 mA) samples were immersed. (j) Diagram showing the mechanism resulting in H^+-responsive hole release from degenerate LDH films.

testing, the OCP of LDH films in the nondegenerate state was relatively low (−0.2 V for LDH(-3 mA) and 0 V for LDH(0 mA)), while the films in the degenerate state (LDH(1 mA) and LDH(3 mA)) exhibited OCPs as high as 0.8 V owing to the accumulation of positively charged holes on the sample surfaces. With prolonged immersion time, no obvious variation in the OCP was detected in the nondegenerate LDH films, while the OCPs of the degenerate LDHs gradually decreased, indicating continuous release of holes stored in the degenerate LDH films. With the release of holes, the degenerate LDH films are expected to gradually transform into the nondegenerate state. To investigate the transformation process, the alteration of EIS spectra of degenerate LDH(3 mA) samples immersed in water was measured. Fig. 6b shows the change in the phase angle with time. At the beginning of the test, only one obvious peak centered at approximately 1000 Hz existed, which is the characteristic feature of highly conductive degenerate LDH films. After immersion for 300 min, another peak centered at approximately 0.1 Hz appeared, causing the phase angle curve to show the typical pattern of nondegenerate LDH films. The impedance alteration is shown in Fig. 6c. The impedance of the system in the low-frequency region sharply increased at the beginning of the tests since the electrolyte had not completely penetrated the sample surfaces, and the existence of air increased the sample impedance. After 100 min of immersion, the

system reached a steady-state and presented a low impedance (10^3–10^4 Ω), suggesting that the LDH(3 mA) sample was in a degenerate state. Three hundred minutes later, the impedance gradually approached 10^5 Ω, verifying that the sample had transformed into a nondegenerate state. The time-dependent EIS data of the degenerate LDH(3 mA) sample were further analyzed by DRT transformation and construction of a two-dimensional correlation spectrum. A crossing peak near the position of (0.1 Hz, 1000 Hz) could be detected in the synchronous spectrum (Fig. 6d), and the peak value was negative, indicating that the responsiveness of the system at 0.1 Hz (ion diffusion process) and that at 1000 Hz (electron transfer process) were coupled and showed opposite patterns of change. This result is consistent with the fact that the peak corresponding to the electron transfer process was the strongest in the DRT spectra of degenerate LDH films, while the peak corresponding to the ion diffusion process was the strongest in the DRT spectra of nondegenerate LDH films (Fig. 5f). In the two-dimensional asynchronous correlation spectrum (Fig. 6e), a positive peak centered around (10 Hz, 0.1 Hz) can be detected, indicating that the hole diffusion process (10 Hz) occurred before ion diffusion (0.1 Hz). The negative peak centered around (1000 Hz, 0.1 Hz) suggested that the ion diffusion process (0.1 Hz) occurred before electron transfer (1000 Hz). Therefore, charge transfer between the degenerate LDH films and the environment occurred in the following sequence: first, holes diffused from the interior of the degenerate LDH films to the interface; then, active ions diffused to the interface; and finally, electron transfer occurred between the holes and the active ions in the microenvironment. Holes in the degenerate films gradually decreased, consequently transforming the films into a nondegenerate state.

The release rate of holes in the degenerate LDH films is related to the kinds of ions in the microenvironment. Unfortunately, it is impractical to investigate the influence of individual ions on the hole release rate since counter ions must be existed to keep the electric neutrality of the electrolyte. Therefore, we have configured a series of solutions containing different kinds of cations and anions, and the cations or anions are in consistent with one another. Then the influence of different ions on the hole releasing rate can be investigated by comparing the electrolyte with similar counter ions. For example, HCl and KCl present the same anions, therefore the difference in charge release rate can be attributed to the differences in cations. We immersed degenerate LDH(3 mA) samples in different electrolytes and measured the OCP. The results showed that the sample immersed in the electrolyte containing HCl showed a fast potential decrease rate, while nearly no potential decrease could be detected for the sample immersed in KOH solution (Fig. 6f, Supplementary Fig. S13). Samples immersed in NaF, NaCl, and KCl solutions showed similar potential decrease rates, lower than that in HCl but much higher than that in KOH solution. These results illustrated that the pH may play an important role in regulating hole transfer. We further immersed degenerate LDH(3 mA) samples in electrolytes with pH values of 4, 6, 7, and 8. The pH value of the electrolyte was adjusted by HCl and KOH since their counter ions exhibit little effect on the charge releasing rate (Fig. S13). The potential decrease rate slowed with increasing pH value, indicating the charge release rate increased with H^+ concentration in the microenvironment (Fig. 6g). EIS spectra of LDH(3 mA) samples immersed in different solutions showed that a smaller impedance arc could be detected for samples immersed in electrolytes with higher pH values (Fig. 6h), and the impedance of LDH(3 mA) increased when it was immersed in electrolytes with low pH values (Supplementary Fig. S14). In addition, the O_2 production rate was also reduced with a higher pH value (Fig. 6i). According to the above results, degenerate LDH films can be gradually transformed into a nondegenerate state. The transformation rate depends on the pH of the microenvironment, and a low pH would result in a high transformation rate, thus leading to a high hole release rate. The hole-release-promotion ability of H^+ ions might derive from their small radius and high mobility. As depicted in Fig. 6j, a Ni vacancy is negatively charged; thus, positively charged ions in the electrolyte tend to flow to the vacancy owing to the electrostatic attraction (Figs. 6j-1). Among all the positively charged ions, H^+ ions present the smallest radius, and they can move freely in LDH films. H^+ ions have been reported to be the major charge carriers in LDHs [48]. With the hydrogen ions flowing from their original sites to the Ni vacancies, holes in the vacancies are transported to the bonded –OH (Figs. 6j-2), which leads to the generation of more free H^+ ions. The newly formed free ions can continue to be transported in the lattice, thus accelerating hole flow in the degenerate LDH films (Figs. 6j-3). A lower pH will increase the concentration of H^+ ions, thus promoting hole release in degenerate LDH films.

3.4. Selective tumor and bacterial inhibition effect of degenerate LDH films

Various cellular behaviors of cancer cells and normal cells cultured on different samples were evaluated. The viabilities of the cells were evaluated by an alamarBlue kit, and the results are shown in Figs. 7a-1 and Figs. 7b-1. Compared to NiTi, the constructed LDH films inhibited the growth of both types of cells, which is following our previous report [36]. After 1 day of cultivation, the viabilities of both cancer cells and normal cells showed similar trends: LDH(-3 mA) > LDH(0 mA) ≈ LDH(1 mA) ≈ LDH(3 mA). When the cultivation time was prolonged to 4 days and 7 days, cancer cells and normal cells reacted differently to the LDH films in the degenerate and nondegenerate states. For cancer cells, cells cultured on nondegenerate samples (LDH(0 mA)) presented the highest viabilities, whereas degenerate LDH films could effectively inhibit the growth of cancer cells. In particular, the viability of cells on LDH(3 mA) decreased with cultivation time, indicating that degenerate LDH films could kill cancer cells. In contrast, degenerate LDH films presented fewer adverse effects on normal cells. The viability of normal cells cultured on degenerate LDH(1 mA) samples was the highest among all LDH samples. Although the viability of normal cells cultured on the LDH(3 mA) samples was lower than that of the other groups, the viability continued to increase with time, suggesting that the degenerate LDH(3 mA) samples showed no toxicity to normal cells.

The live/dead staining images of cancer cells and normal cells cultured on various samples for 4 days confirmed the selective cancer cell killing ability of the degenerate LDH films (Figs. 7a-2 and Figs. 7b-2). Concerning cancer cells, the largest number of live cells (stained green) was observed on the nondegenerate LDH(0 mA) samples, the cell number was obviously decreased on the degenerate LDH(1 mA) and LDH(3 mA) samples, and many dead cells were detected on the degenerate LDH(3 mA) samples, whereas normal cells grew well on the degenerate LDH(1 mA) samples. Although some dead normal cells also appeared on the degenerate LDH(3 mA) samples, the density of live normal cells was higher than that of cancer cells cultured on LDH(3 mA).

The cell viability can also be reflected by the cellular morphology. Live cells usually present a large spread area and possess large amounts of pseudopodia; necrotic cells are characterized by ruptured cell membranes; cells in the early apoptotic state are spindle in shape; and apoptotic cells further shrink to a ball-like shape. The morphology of cells cultured on various samples was observed via scanning electron microscopy (SEM) (Figs. 7a-3, Figs. 7b-3), cells in different states were marked with different colors, and the percentages of cells in various states were calculated (Figs. 7a-4, Figs. 7b-4). Approximately 82% of cancer cells on the nondegenerate LDH(0 mA) samples were in the live state, while this value decreased to 47% and 4% on the degenerate LDH (1 mA) and LDH(3 mA) samples, respectively. In addition, the percentages of cells in the early apoptotic state and apoptotic state on degenerate LDH films increased compared to those cultured on nondegenerate samples; only 7% of cells were in the early apoptotic state and 9% of cells were in the apoptotic state on LDH(0 mA), while the percentages increased to 56% and 36% for cancer cells cultured on LDH(3 mA), verifying the effective cancer cell killing ability of LDH films in the degenerate state. In contrast, the degenerate LDH films presented less inhibitory effects on normal cells: the apoptosis percentage of normal

cells cultured on LDH(0 mA) was 12%, and it decreased to 5% for cells cultured on LDH(1 mA). On LDH(3 mA), the apoptosis percentage of normal cells slightly increased to 26%, much lower than that for cancer cells.

The apoptotic states of cells cultured on different samples were further characterized by JC-1 staining. The results showed that LDH films in a degenerate state promoted apoptosis of cancer cells but presented fewer adverse effects on normal cells (Supplementary Fig. S15). Flow cytometry results showed that most of the cancer cells on the nondegenerate LDH films were intact, while numerous cell debris appeared on the degenerate LDH films, further confirming the cancer cell killing ability of the degenerate LDH films (Supplementary Fig. S16). The expression of apoptosis-related genes in cells cultured on various samples was evaluated by RT-PCR (Fig. 7c). It can be found that the trend of mRNA expression of Caspase-3 was not corresponded with that of Bcl-2, owning to the complex interaction between the two genes. Some studies stressed that Bcl-2 is the upstream regulator of Caspase-3, some argued that the two genes may be relatively independent in the regulation of apoptosis [49]. The apoptosis promotion ability of different samples can be reflected by the ratio between the proapoptotic gene Caspase-3 and the antiapoptotic gene Bcl-2. A much higher Caspasase-3/Bcl-2 ratio (4–6) was detected in cancer cells cultured on degenerate LDH films compared to those cultured on nondegenerate LDH films (approximately 0.4). In contrast, the Caspasase-3/Bcl-2 ratio stayed at a relatively low level for normal cells cultured on different samples. These results indicated that degenerate LDH films present preferable selective cancer cell inhibition ability.

In addition, the degenerate LDH films possessed the ability to inhibit the migration of cancer cells, as shown in Supplementary Fig. S17. Malignant metastasis is the major cause of death for cancer patients. The migration inhibition capacity of degenerate LDH films is expected to further improve treatment outcomes.

Encouraged by the preferable *in vitro* results, the selective antitumor effects of degenerate LDH films were further evaluated *in vivo*. Tumor-bearing nude mice were divided into three groups. Compared to the control group implanted with NiTi, both groups implanted with LDH(0 mA) and LDH(3 mA) showed inhibited tumor growth (Fig. 8a, Fig. 8b). In particular, the LDH(3 mA) samples almost completely inhibited

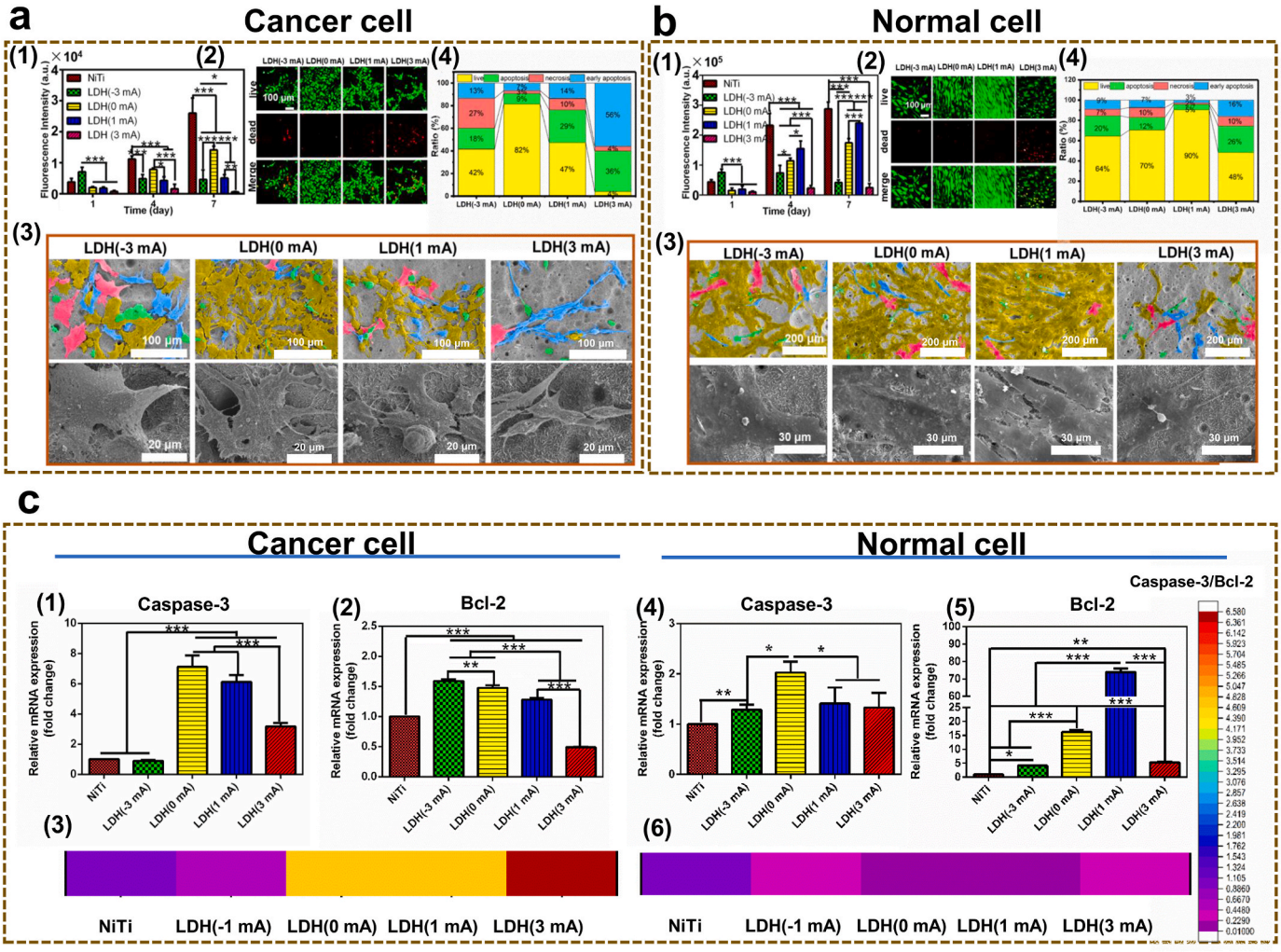

Fig. 7. *In vitro* selective cancer cell inhibition ability of degenerate LDH films. (a) Viability of cancer cells: proliferation of cancer cells cultured on various samples, n = 4 (a-1); live/dead stained cancer cells cultured on various samples (a-2); SEM images of cancer cells cultured on various samples, in which cells are marked by yellow (live), green (apoptotic), red (necrotic) and blue (early apoptotic) based on their survival state (a-3); percentages of cancer cells in different states acquired from the SEM images (a-4). (b) Viability of normal cells: proliferation of normal cells cultured on various samples, n = 4 (b-1); live/dead stained normal cells cultured on various samples (b-2); SEM images of normal cells cultured on various samples, in which cells were marked by yellow (live), green (apoptotic), red (necrotic) and blue (early apoptotic) based on their survival state (b-3); percentages of normal cells in different states acquired from the SEM images (b-4). (c) Expression of apoptosis-related genes in cancer cells and normal cells cultured on various samples: relative mRNA expression of Caspase-3 (c-1) and Bcl-2 (c-2) and ratio of Caspase-3/Bcl-2 (c-3) in cancer cells cultured on various samples; relative mRNA expression of Caspase-3 (c-4) and Bcl-2 (c-5) and ratio of Caspase-3/Bcl-2 (c-6) in normal cells cultured on various samples, n = 3.

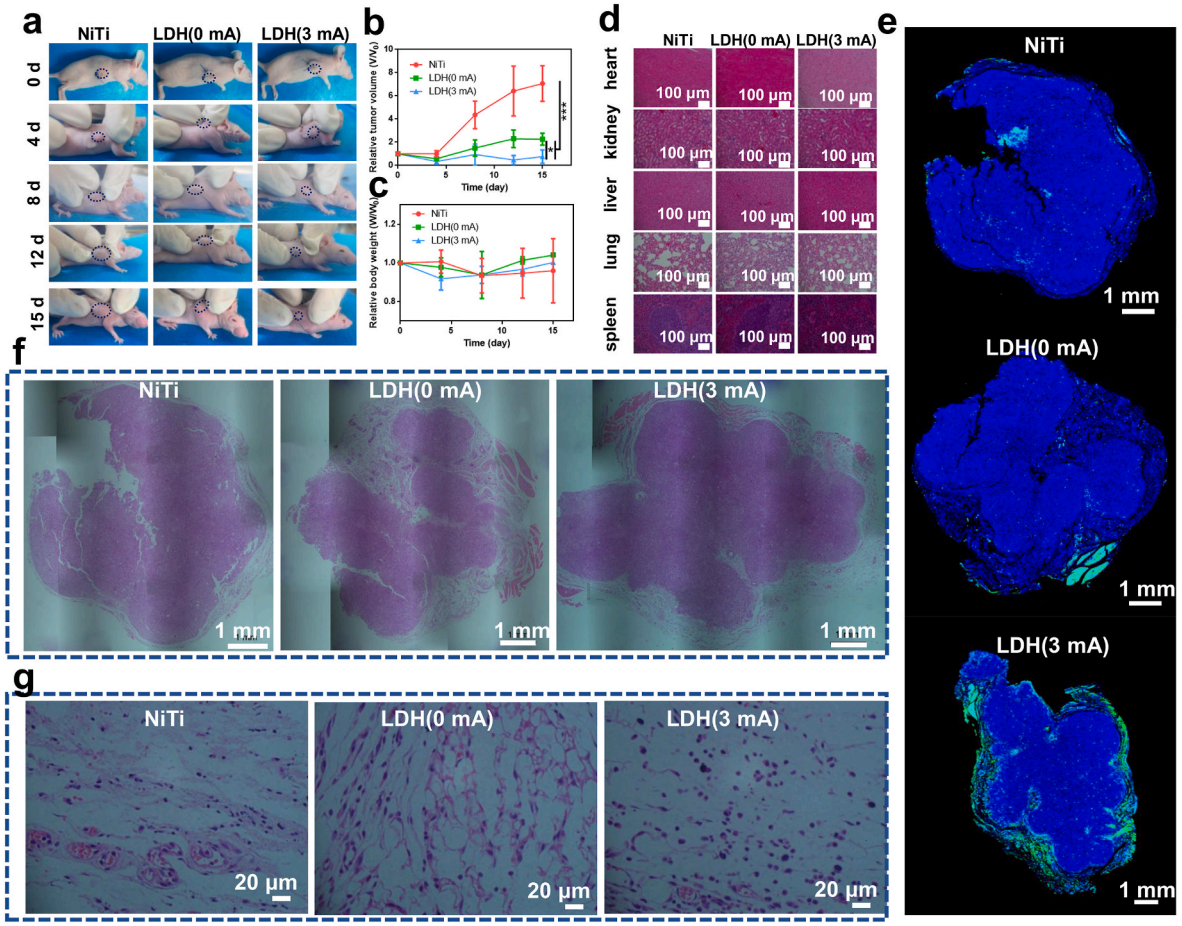

Fig. 8. *In vivo* tumor-inhibition effect of degenerate LDH films. (a) Representative photos of tumor-bearing mice after being implanted with NiTi, LDH(0 mA) and LDH(3 mA) samples for various time periods. (b) Relative tumor volumes of mice implanted with NiTi, LDH(0 mA) and LDH(3 mA) samples, n = 4. (c) Relative body weights of mice after being implanted with NiTi, LDH(0 mA) and LDH(3 mA) samples for various time periods, n = 4. (d) Images of H&E-stained spleen, lung, liver, kidney and heart tissue in mice implanted with NiTi, LDH(0 mA) and LDH(3 mA) samples. (e) Images of TUNEL-stained tumor tissue in mice implanted with NiTi, LDH(0 mA) and LDH(3 mA) samples. (f) Images of H&E-stained tumor tissue in mice implanted with NiTi, LDH(0 mA) and LDH(3 mA) samples. (g) Magnified images showing the periphery of the tumor tissue in mice implanted with NiTi, LDH(0 mA) and LDH(3 mA) samples.

tumor growth, which was visually confirmed by comparing the tumor sizes shown in Supplementary Fig. S18. In addition, the body weights of the mice in different groups did not show any noticeable changes (Fig. 8c). Routine blood examination and hematoxylin-eosin (H&E) staining of the spleen, lung, liver, kidney, and heart were conducted 15 days after sample implantation. Few differences could be detected among the different groups. All tissues were in a healthy state (Fig. 8d), and routine blood examination items and all blood biochemical indices of the experimental animals were within norms (Supplementary Fig. S19), illustrating satisfactory *in vivo* biocompatibility and biosafety of the degenerate LDH films.

Terminal deoxynucleotidyl transferase-mediated dUTP nick end labeling (TUNEL) staining of tumor tissue sections was conducted to investigate the *in vivo* tumor cell killing ability of various samples, and the results are presented in Fig. 8e and Supplementary Fig. S20. Nearly no dead tumor cells (stained green) were observed from the tumors contacting NiTi and LDH(0 mA), whereas all cells in the periphery of the tumors contacting the LDH(3 mA) samples were in apoptotic states, but the interior tumor cells were still alive. These results indicated that the degenerate LDH films present effective *in vivo* tumor-killing ability for contacted tumor tissue, while they possess no long-distance antitumor capacity. The images of H&E-stained tumor tissue confirmed the above conclusion. Cells in the interior and periphery of tumors presented different cellular morphologies. In the interior of tumors, cells were densely packed, and no obvious differences could be detected among the tumor tissues in contact with different samples (Fig. 8f, Supplementary Fig. S21). In the periphery, cells were loosely packed, and most of the cells contacting NiTi and LDH(0 mA) were polygonal in shape, whereas the cells contacting LDH(3 mA) shrunk to a spindle- or ball-like shape, which are the characteristic morphology of apoptotic cells (Fig. 8g). The *in vivo* results indicated that degenerate LDH films can kill the tumor cells in a layer-by-layer way just like the way we peel the layers of onions. After the outermost layer of tumor cells were killed, the inside tumor cells were exposed to the films. Therefore, the degenerate LDH film can gradually lead to tumor ablation.

Bacterial infection is another serious issue leading to metallic implant failure [50,51]. The antibacterial effect of the degenerate LDH films was evaluated. The viabilities of *S. aureus*, *E. coli*, and *P. aeruginosa* cultured on degenerate LDH(3 mA) samples were close to zero (Supplementary Fig. S22). *In vivo* experiments showed that after subcutaneous implantation of *S. aureus*-contaminated samples for 1 day, many bacterial colonies appeared on the agar plates of the NiTi group and LDH group, whereas the number of bacterial colonies was obviously reduced in the LDH(3 mA) group (Supplementary Fig. S23). In addition, the tissues in contact with the sample surface were stained by H&E and observed by optical microscope (Supplementary Fig. S24), the thickness of the fibrous layer and number of infiltration inflammatory cells in the LDH(3 mA) group were much smaller than the other groups, showing the good *in vivo* antibacterial capacity of the degenerate LDH(3 mA) samples.

Such preferable selective tumor and bacterial killing abilities may result from the H^+-related hole-release properties of the degenerate LDH films. As discussed above, holes stored in degenerate LDHs can be released into the environment, and the released holes present high oxidation ability, which can destroy the cell membrane and ultimately kill cells and bacteria. However, the cell and bacterial killing abilities of the degenerate LDH films are determined by the hole release rate. A high hole release rate leads to a burst increase in oxidative stress and results in cell death, whereas when the hole release rate is slow, the strong oxidizing substance induced by holes is metabolized before the redox microenvironment becomes unbearable for cells [52]. The hole release rate of the degenerate LDH films is positively correlated with the H^+ concentration in the microenvironment. Fortunately, tumor- and bacteria-related infections lower the local pH [53,54]. Tumor tissues are rich in H^+ ions and present a low pH owing to the "Warburg effect" [55–57], which accelerates the release of holes in degenerate LDHs. Holes released from the degenerate LDH films exhibit high oxidation ability and can react with the physiological environment to produce reactive oxygen species (ROS). It can be found that more ROS exists in cancer cells cultured on the degenerate LDH films (Supplementary Fig. S25). The increase of ROS cussed nucleus deformation, which activated the apoptosis pathway, resulting in the downregulation of anti-apoptosis proteins Bcl-2. The expressed pro-apoptosis protein would then bond to the mitochondria surface, resulting in holes formed across the mitochondria membrane. Thereafter, mitochondria membrane potential decreases, and permeation increases, leading to the release of apoptosis cytokines. The apoptosis cytokines activated Caspase 3, which cut more than 100 substrates, and finally resulted in cell apoptosis. Similarly, the bacteria were also killed by the ROS induced by the rapid release of holes from degenerate LDH films. In contrast, when in contact with normal tissue, the relatively high local pH slows down the hole release; hence, the degenerate LDH films cause little harm to normal tissues.

3.5. Cyclic transformation of LDH films between nondegenerate and degenerate states

The degenerate LDH films automatically transformed into a nondegenerate state by releasing positively charged holes stored in the films. The holes can also be exhausted by directly applying a negative voltage to the films. Therefore, LDH films can be artificially transformed between degenerate and nondegenerate states via charging and discharging treatments, which can be verified by OCP and water contact measurements. The degenerate LDH films possessed a high OCP and a low water contact angle owing to the accumulation of electron holes on the sample surfaces. As shown in Fig. 9a, after charging and discharging treatments, the OCP and water contact angle varied cyclically, indicating the successful transformation of LDHs between degenerate and nondegenerate states. After several cycles, the plate-like structures of the films were not destroyed (Supplementary Fig. S26), and the preferable biological effect of LDHs in the degenerate state was maintained.

We investigated the antibacterial ability of LDH films after cyclic charging and discharging treatments. Fig. 9b presents photos of recultivated colonies of *E. coli* dissociated from different samples, and the number of colonies was counted. Many bacterial colonies could be found on the LDH films in the nondegenerate state, whereas nearly no bacterial colonies could be detected in the degenerate LDH groups. CLSM images of live/dead-stained bacteria are shown in Fig. 9c. Most bacteria on nondegenerate LDH films were in the live state (stained green), while numerous dead bacteria (stained red) appeared on LDH films in the degenerate state. SEM images of *E. coli* further confirmed the above results (Fig. 9d). Many *E. coli* could be detected on the surface of nondegenerate LDH films, while few *E. coli* could be found on degenerate LDH films. In addition, the bacteria detected on degenerate LDH films showed a broken membrane, suggesting that they were dying. A similar cyclic appearance of the inhibition effect of LDH films on *S. aureus*, *P. aeruginosa*, and cancer cells (Supplementary Fig. S27, Fig. S28) was also observed. These results indicate that the transformation between degenerate and nondegenerate states of LDHs can be cycled. This inspired us to conclude that the selective antitumor and antibacterial effects of degenerate LDHs are not a one-off event.

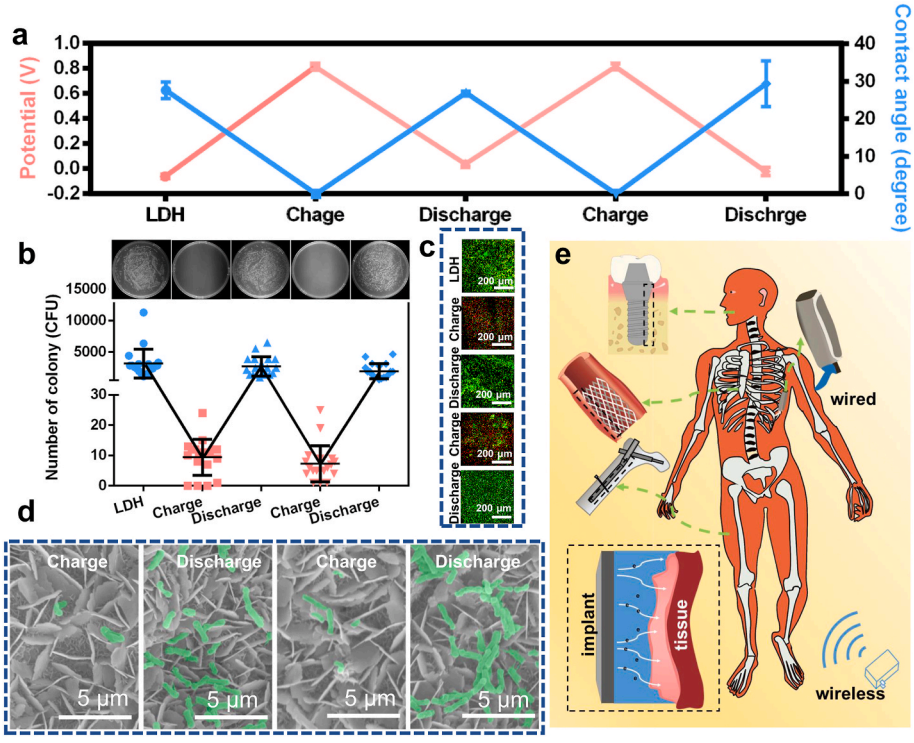

Fig. 9. Cyclic transformation of LDH films between nondegenerate and degenerate states. (a) OCP and water contact angle of LDH films after cyclic charging and discharging treatments, n = 3. (b) Photos of recultivated *E. coli* dissociated from various samples and corresponding colony number, n = 3. (c) Live/dead stained *E. coli* cultured on various samples. (d) SEM images of *E. coli* cultured on various samples. (e) Scheme illustrating the possible application of degenerate LDH films in the surface modification of various implants, realizing dynamic and selective regulation of the biological behavior in a long-lasting manner by coupling with wired and wireless power supplies.

It's the future trend to design medical devices with electric current transmission abilities [58]. Many types of electronic implants have already been developed and widely used in neurosurgery, cardiology, orthopedics, stomatology, etc. However, the biosafety concern and complex design of these electronic devices limit their *in vivo* application. In this study, we focused on the LDH films which show promising application in biomedical areas owning to their high biocompatibility. In addition, the degenerate LDH films can be easily constructed on a series of metallic implants, rendering the implants become "smart" without huge structure modification (Fig. 9e), which is a benefit for their industrial transformation. With the development of implantable batteries or wireless charging technologies, the designed degenerate LDH films may endow different types of implants (such as the dental implant, orthopedic implants, stents, etc.) with long-lasting selective antitumor and antibacterial effects.

4. Conclusions

We show a proof-of-concept study that degenerate LDH modified implants can selectively induce the death of cancer cells and bacteria by electrocution in a microenvironment-responsive manner. The film can gradually release charges and transform into a nondegenerate state. The charge release rate depends on the H^+ concentration in the microenvironment. In the acidic tumor or infection microenvironment, the degenerate LDH film is quickly discharged, and the sharp release of holes can effectively kill cancer cells and bacteria. However, when cultured with normal cells, the discharge rate is slow, and the prepared films cause less harm to normal cells. In addition, the transformation between the degenerate state and the nondegenerate state of the LDH film can be cycled. If coupled with an energy supply in a wired or wireless manner, the constructed film might exhibit durable selective and self-adjustable biological effects to meet the dynamic requirements of tissue contact with implants.

In the context of clinical practice, postoperative cancer patients are not fit for immediate chemotherapy or radiotherapy due to their extremely poor condition, which provides an opportunity for cancer cells to proliferate and metastasize, resulting in a high recurrence rate. The surface-modified implants reported in this study allow a new pattern of electrotherapy, which functions in a microenvironment-responsive manner. Compared with traditional chemotherapy or radiotherapy, the newly designed electrotherapy shows much lower adverse effects on normal tissues without scarifying the therapeutic efficiency. In addition, they function immediately after the implantation operation, rendering the residual cancer cells killed in the bud condition, minimizing the cancer recurrence rate.

Data availability

The main data supporting the findings of this study are available within the paper and its Supplementary Information. Additional data are available from the corresponding authors upon reasonable request.

CRediT authorship contribution statement

Donghui Wang: Conceptualization, Formal analysis, Writing – original draft, Writing – review & editing. **Shun Xing:** Data curation, Investigation, Writing – review & editing. **Feng Peng:** Data curation, Methodology, Writing – original draft. **Xianming Zhang:** Data curation, Validation. **Ji Tan:** Methodology. **Xueqing Hao:** Visualization. **Yuqin Qiao:** Validation. **Naijian Ge:** Conceptualization, Funding acquisition. **Xuanyong Liu:** Conceptualization, Funding acquisition, Project administration.

Declaration of competing interest

The authors declare that they have no known competing financial interests or personal relationships that could have appeared to influence the work reported in this paper.

Acknowledgement

This work received financial support from the National Key R&D Program of China (2021YFC2400500), National Natural Science Foundation of China (31971249, 51901239), Science and Technology Commission of Shanghai Municipality (19JC1415500, 20S31903300), and Natural Science Foundation of Hebei Province of China (E2021202001), High-level full-time talents project of Guangdong Provincial People's Hospital (KY012021462). The authors gratefully acknowledge the support from the beamline BL14W1 at Shanghai Synchrotron Radiation Facility for the X-ray absorption spectroscopy characterization.

Appendix A. Supplementary data

Supplementary data to this article can be found online at https://doi.org/10.1016/j.bioactmat.2022.06.004.

References

[1] G.R. Dagenais, D.P. Leong, S. Rangarajan, F. Lanas, P. Lopez-Jaramillo, R. Gupta, R. Diaz, A. Avezum, G.B.F. Oliveira, A. Wielgosz, S.R. Parambath, P. Mony, K. F. Alhabib, A. Temizhan, N. Ismail, J. Chifamba, K. Yeates, R. Khatib, O. Rahman, K. Zatonska, K. Kazmi, L. Wei, J. Zhu, A. Rosengren, K. Vijayakumar, M. Kaur, V. Mohan, A. Yusufali, R. Kelishadi, K.K. Teo, P. Joseph, S. Yusuf, Variations in common diseases, hospital admissions, and deaths in middle-aged adults in 21 countries from five continents (PURE): a prospective cohort study, Lancet 395 (10226) (2020) 785–794.

[2] L.T. Tchelebi, C. Eng, C.A. Messick, T.S. Hong, E.B. Ludmir, L.A. Kachnic, N. G. Zaorsky, Current treatment and future directions in the management of anal cancer, CA-Cancer, J. Clin. (2021).

[3] C. Zhu, M. He, D. Sun, Y. Huang, L. Huang, M. Du, J. Wang, J. Wang, Z. Li, B. Hu, Y. Song, Y. Li, G. Feng, L. Liu, L. Zhang, 3D-Printed multifunctional polyetheretherketone bone scaffold for multimodal treatment of osteosarcoma and osteomyelitis, ACS Appl. Mater. Interfaces 13 (40) (2021) 47327–47340.

[4] C. Bastiancich, A. Malfanti, V. Preat, R. Rahman, Rationally designed drug delivery systems for the local treatment of resected glioblastoma, Adv. Drug Deliv. Rev. 177 (2021).

[5] E. Gauto, J.D.C. Fratti, M. Salazar, H. Macchi, S.U.U. Banskota, B. Baral, C. Weir, K. Ahuja, J.A. Cattoni, In-hospital outcomes of percutaneous coronary intervention with drug-eluting stent in patients with localized and metastatic cancer, J. Clin. Oncol. 39 (15) (2021).

[6] A. Alzanbagi, L. Ahmed, M. Fatani, H. Alaidarous, I. Ahmed, A. Tashkandi, M. Khan, A. Algesry, M. Shariff, Self-expanding metallic stent for palliation of malignant colorectal cancer: a single tertiary referral center experience, Gut 70 (2021). A129-A129.

[7] S. Piperno-Neumann, M.-C. Le Deley, F. Redini, H. Pacquement, P. Marec-Berard, P. Petit, H. Brisse, C. Lervat, J.-C. Gentet, N. Entz-Werle, A. Italiano, N. Corradini, E. Bompas, N. Penel, M.-D. Tabone, A. Gomez-Brouchet, J.-M. Guinebretiere, E. Mascard, F. Gouin, A. Chevance, N. Bonnet, J.-Y. Blay, L. Brugieres, U. Sarcoma Grp, S. French Soc Pediatric Oncology, G.-G. French Sarcoma Grp, Zoledronate in combination with chemotherapy and surgery to treat osteosarcoma (OS2006): a randomised, multicentre, open-label, phase 3 trial, Lancet Oncol. 17 (8) (2016) 1070–1080.

[8] T. Yamamoto, K. Miyashita, K. Shimada, T. Sekikawa, Y. Uto, T. Nunoue, Y. Kaga, Y. Kitahara, Y. Saito, K. Kobayashi, E. Kinugasa, Efficacy of chemotherapy after self-expanding metal stent placement for gastric outlet obstruction caused by an unresectable malignant tumor, J. Clin. Oncol. 33 (3) (2015).

[9] E.P.W. Jenkins, A. Finch, M. Gerigk, I.F. Triantis, C. Watts, G.G. Malliaras, Electrotherapies for glioblastoma, Adv. Sci. 8 (18) (2021).

[10] A. Hills, J. Stebbing, Electrotherapy: enlightening modern medicine, Lancet Oncol. 15 (10) (2014) 1060–1061.

[11] E.H. Ledet, B. Liddle, K. Kradinova, S. Harper, Smart implants in orthopedic surgery, improving patient outcomes: a review, Inov. Entrep. health 5 (2018) 41–51.

[12] A.H. Rajabi, M. Jaffe, T.L. Arinzeh, Piezoelectric materials for tissue regeneration: a review, Acta Biomater. 24 (2015) 12–23.

[13] C. Li, Y. Li, T. Yao, L. Zhou, C. Xiao, Z. Wang, J. Zhai, J. Xing, J. Chen, G. Tan, Y. Zhou, S. Qi, P. Yu, C. Ning, Wireless electrochemotherapy by selenium-doped piezoelectric biomaterials to enhance cancer cell apoptosis, ACS Appl. Mater. Interfaces 12 (31) (2020) 34505–34513.

[14] W. Zhang, N. Liu, H. Shi, J. Liu, L. Shi, B. Zhang, H. Wang, J. Ji, P.K. Chu, Upregulation of BMSCs osteogenesis by positively-charged tertiary amines on polymeric implants via charge/iNOS signaling pathway, Sci. Rep. 5 (2015).

[15] G. Wang, H. Feng, L. Hu, W. Jin, Q. Hao, A. Gao, X. Peng, W. Li, K.-Y. Wong, H. Wang, Z. Li, P.K. Chu, An antibacterial platform based on capacitive carbon-

doped TiO_2 nanotubes after direct or alternating current charging, Nat. Commun. 9 (2018).
[16] J. Tian, R. Shi, Z. Liu, H. Ouyang, M. Yu, C. Zhao, Y. Zou, D. Jiang, J. Zhang, Z. Li, Self-powered implantable electrical stimulator for osteoblasts' proliferation and differentiation, Nano Energy 59 (2019) 705–714.
[17] W. Guo, X. Zhang, X. Yu, S. Wang, J. Qiu, W. Tang, L. Li, H. Liu, Z.L. Wang, Self-powered electrical stimulation for enhancing neural differentiation of mesenchymal stem cells on graphene-poly(3,4-ethylenedioxythiophene) hybrid microfibers, ACS Nano 10 (5) (2016) 5086–5095.
[18] A. Wang, M. Hu, L. Zhou, X. Qiang, Self-powered well-aligned P(VDF-TrFE) piezoelectric nanofiber nanogenerator for modulating an exact electrical stimulation and enhancing the proliferation of preosteoblasts, Nanomaterials 9 (3) (2019).
[19] R. Hinchet, H.-J. Yoon, H. Ryu, M.-K. Kim, E.-K. Choi, D.-S. Kim, S.-W. Kim, Transcutaneous ultrasound energy harvesting using capacitive triboelectric technology, Science 365 (6452) (2019) 491.
[20] J. Charthad, M.J. Weber, T.C. Chang, A. Arbabian, A mm-sized implantable medical device (IMD) with ultrasonic power transfer and a hybrid bi-directional data link, IEEE Solid-St. Circ. 50 (8) (2015) 1741–1753.
[21] L. Radziemski, I.R.S. Makin, In vivo demonstration of ultrasound power delivery to charge implanted medical devices via acute and survival porcine studies, Ultrasonics 64 (2016) 1–9.
[22] M. Alam, S. Li, R.U. Ahmed, Y.M. Yam, S. Thakur, X.-Y. Wang, D. Tang, S. Ng, Y.-P. Zheng, Development of a battery-free ultrasonically powered functional electrical stimulator for movement restoration after paralyzing spinal cord injury, J. NeuroEng. Rehabil. 16 (2019).
[23] D.K. Piech, B.C. Johnson, K. Shen, M.M. Ghanbari, K.Y. Li, R.M. Neely, J.E. Kay, J. M. Carmena, M.M. Maharbiz, R. Muller, A wireless millimetre-scale implantable neural stimulator with ultrasonically powered bidirectional communication, Nat. Biomed. Eng. 4 (2) (2020) 207–222.
[24] M.S. Mannoor, H. Tao, J.D. Clayton, A. Sengupta, D.L. Kaplan, R.R. Naik, N. Verma, F.G. Omenetto, M.C. McAlpine, Graphene-based wireless bacteria detection on tooth enamel, Nat. Commun. 3 (2012).
[25] D.K. Freeman, J.M. O'Brien, P. Kumar, B. Daniels, R.A. Irion, L. Shraytah, B. K. Ingersol, A.P. Magyar, A. Czarnecki, J. Wheeler, J.R. Coppeta, M.P. Abban, R. Gatzke, S.I. Fried, S.W. Lee, A.E. Duwel, J.J. Bernstein, A.S. Widge, A. Hernandez-Reynoso, A. Kanneganti, M.I. Romero-Ortega, S.F. Cogan, A sub-millimeter, inductively powered neural stimulator, Front. Neurosci. 11 (2017).
[26] L.Y. Maeng, M.F. Murillo, M. Mu, M.-C. Lo, M. de la Rosa, J.M. O'Brien, D. K. Freeman, A.S. Widge, Behavioral validation of a wireless low-power neurostimulation technology in a conditioned place preference task, J. Neural. Eng. 16 (2) (2019).
[27] A. Singer, S. Dutta, E. Lewis, Z.Y. Chen, J.C. Chen, N. Verma, B. Avants, A. K. Feldman, J. O'Malley, M. Beierlein, C. Kemere, J.T. Robinson, Magnetoelectric materials for miniature, wireless neural stimulation at therapeutic frequencies, Neuron 107 (4) (2020) 631.
[28] M. Filippi, B. Dasen, J. Guerrero, F. Garello, G. Isu, G. Born, M. Ehrbar, I. Martin, A. Scherberich, Magnetic nanocomposite hydrogels and static magnetic field stimulate the osteoblastic and vasculogenic profile of adipose-derived cells, Biomaterials (2019) 223.
[29] A.R. Tomas, A.I. Goncalves, E. Paz, P. Freitas, R.M.A. Domingues, M.E. Gomes, Magneto-mechanical actuation of magnetic responsive fibrous scaffolds boosts tenogenesis of human adipose stem cells, Nanoscale 11 (39) (2019) 18255–18271.
[30] W. Shi, J. Huang, R. Fang, M. Liu, Imparting Functionality to the Hydrogel by magnetic-field-induced nano-assembly and macro-response, ACS Appl. Mater. Interfaces 12 (5) (2020) 5177–5194.
[31] E. Boedtkjer, S.F. Pedersen, The Acidic Tumor Microenvironment as a Driver of Cancer, in: M.T. Nelson, K. Walsh (Eds.), Annu. Rev. of Physiol. 822020 103-126.
[32] A.B. Cook, P. Decuzzi, Harnessing endogenous stimuli for responsive materials in theranostics, ACS Nano 15 (2) (2021) 2068–2098.
[33] P. Pan, Q. Yue, J. Li, M. Gao, X. Yang, Y. Ren, X. Cheng, P. Cui, Y. Deng, Smart cargo delivery system based on mesoporous nanoparticles for bone disease diagnosis and treatment, Adv. Sci. 8 (12) (2021).
[34] N.U. Dharmaratne, A.R. Kaplan, P.M. Glazer, Targeting the hypoxic and acidic tumor microenvironment with ph-sensitive peptides, Cells 10 (3) (2021).
[35] D. Wang, N. Ge, T. Yang, F. Peng, Y. Qiao, Q. Li, X. Liu, NIR-Triggered crystal phase transformation of NiTi-layered double hydroxides films for localized chemothermal tumor therapy, Adv. Sci. 5 (4) (2018).
[36] D. Wang, F. Peng, J. Li, Y. Qiao, Q. Li, X. Liu, Butyrate-inserted Ni-Ti layered double hydroxide film for H_2O_2-mediated tumor and bacteria killing, Mater, Today Off. 20 (5) (2017) 238–257.
[37] D. Wang, N. Ge, J. Li, Y. Qiao, H. Zhu, X. Liu, Selective tumor cell inhibition effect of Ni-Ti Layered double hydroxides thin films driven by the reversed ph gradients of tumor cells, ACS Appl. Mater. Interfaces 7 (15) (2015) 7843–7854.
[38] J. Liu, F. Ciucci, The Gaussian process distribution of relaxation times: a machine learning tool for the analysis and prediction of electrochemical impedance spectroscopy data, Electrochim. Acta 331 (2020).
[39] C.R. Arciola, D. Campoccia, L. Montanaro, Implant infections: adhesion, biofilm formation and immune evasion, Nat. Rev. Microbiol. 16 (7) (2018) 397–409.
[40] M. Xu, M. Wei, Layered double hydroxide-based catalysts: recent advances in preparation, structure, and applications, Adv. Funct. Mater. 28 (47) (2018).
[41] J. Yu, Q. Wang, D. O'Hare, L. Sun, Preparation of two dimensional layered double hydroxide nanosheets and their applications, Chem. Soc. Rev. 46 (19) (2017) 5950–5974.
[42] X. Li, M. Xin, S. Guo, T. Cai, D. Du, W. Xing, L. Zhao, W. Guo, Q. Xue, Z. Yan, Insight of synergistic effect of different active metal ions in layered double hydroxides on their electrochemical behaviors, Electrochim. Acta 253 (2017) 302–310.
[43] H. Shen, S.T. Omelchenko, D.A. Jacobs, S. Yalamanchili, Y. Wan, D. Yan, P. Phang, D. The, Y. Wu, Y. Yin, C. Samundsett, J. Peng, N. Wu, T.P. White, G.G. Andersson, N.S. Lewis, K.R. Catchpole, In situ recombination junction between p-Si and TiO_2 enables high-efficiency monolithic perovskite/Si tandem cells, Sci. Adv. 4 (12) (2018).
[44] X. Yu, J. Zhang, Z. Zhao, W. Guo, J. Qiu, X. Mou, A. Li, J.P. Claverie, H. Liu, NiO-TiO_2 p-n heterostructured nanocables bridged by zero-bandgap rGO for highly efficient photocatalytic water splitting, Nano Energy 16 (2015) 207–217.
[45] D. Wang, Q. Li, J. Qiu, X. Zhang, N. Ge, X. Liu, Corrosion motivated ROS generation helps endow titanium with broad-spectrum antibacterial abilities, Adv. Mater. Interfac. 6 (17) (2019).
[46] Z.-z. Yang, C. Zhang, G.-m. Zeng, X.-f. Tan, D.-l. Huang, J.-w. Zhou, Q.-z. Fang, K.-h. Yang, H. Wang, J. Wei, K. Nie, State-of-the-art progress in the rational design of layered double hydroxide based photocatalysts for photocatalytic and photoelectrochemical H_2/O_2 production, Coord. Chem. Rev. 446 (2021).
[47] Y. Sun, S. Sun, X. Liao, J. Wen, G. Yin, X. Pu, Y. Yao, Z. Huang, Effect of heat treatment on surface hydrophilicity-retaining ability of titanium dioxide nanotubes, Appl. Surf. Sci. 440 (2018) 440–447.
[48] Z.H. Li, H.H. Duan, M.F. Shao, J.B. Li, D. O'Hare, M. Wei, Z.L. Wang, Ordered-vacancy-induced cation intercalation into layered double hydroxides: a general approach for high-performance supercapacitors, Chem 4 (9) (2018) 2168–2179.
[49] L.F. Jarskog, E.S. Selinger, J.A. Lieberman, J.H. Gilmore, Apoptotic proteins in the temporal cortex in schizophrenia: high Bax/Bcl-2 ratio without caspase-3 activation, Am. J. Psychiatr. 161 (1) (2004) 109–115.
[50] W. Xi, V. Hegde, S.D. Zoller, H.Y. Park, C.M. Hart, T. Kondo, C.D. Hamad, Y. Hu, A. H. Loftin, D.O. Johansen, Z. Burke, S. Clarkson, C. Ishmael, K. Hori, Z. Mamouei, H. Okawa, I. Nishimura, N.M. Bernthal, T. Segura, Point-of-care antimicrobial coating protects orthopaedic implants from bacterial challenge, Nat. Commun. 12 (1) (2021).
[51] S. Wu, J. Xu, L. Zou, S. Luo, R. Yao, B. Zheng, G. Liang, D. Wu, Y. Li, Long-lasting renewable antibacterial porous polymeric coatings enable titanium biomaterials to prevent and treat peri-implant infection, Nat. Commun. 12 (1) (2021).
[52] N. Kong, H. Zhang, C. Feng, C. Liu, Y. Xiao, X. Zhang, L. Mei, J.S. Kim, W. Tao, X. Ji, Arsenene-mediated multiple independently targeted reactive oxygen species burst for cancer therapy, Nat. Commun. 12 (1) (2021).
[53] S. Yan, H. Shi, L. Song, X. Wang, L. Liu, S. Luan, Y. Yang, J. Yin, Nonleaching bacteria-responsive antibacterial surface based on a unique hierarchical, ACS Appl. Mater. Interfaces 8 (37) (2016) 24471–24481.
[54] D. Lin, X. Feng, B. Mai, X. Li, F. Wang, J. Liu, X. Liu, K. Zhang, X. Wang, Bacterial-based cancer therapy: an emerging toolbox for targeted drug/gene delivery, Biomaterials (2021) 277.
[55] M.V. Liberti, J.W. Locasale, The Warburg effect: how does it benefit cancer cells? Trends Biochem. Sci. 41 (3) (2016) 211–218.
[56] E. Persi, M. Duran-Frigola, M. Damaghi, W.R. Roush, P. Aloy, J.L. Cleveland, R. J. Gillies, E. Ruppin, Systems analysis of intracellular pH vulnerabilities for cancer therapy, Nat. Commun. 9 (2018).
[57] B. Ordway, R.J. Gillies, M. Damaghi, Extracellular acidification induces lysosomal dysregulation, Cells 10 (5) (2021).
[58] D. Wang, J. Tan, H. Zhu, Y. Mei, X. Liu, Biomedical implants with charge-transfer monitoring and regulating abilities, Adv. Sci. 8 (16) (2021).